Effect of aluminate and carbonate in magnesia silicate cement

Ellina Bernard [a,b,*], Barbara Lothenbach [b], Alexander German [b], Daniel Rentsch [c], Frank Winnefeld [b]

[a] Department of Civil and Environmental Engineering, Imperial College London, South Kensington, 11 Skempton Building, London, SW7 2AZ, UK
[b] Empa, Swiss Federal Laboratories for Materials Science and Technology, Laboratory for Concrete and Asphalt, 8600, Dübendorf, Switzerland
[c] Empa, Swiss Federal Laboratories for Materials Science and Technology, Laboratory for Functional Polymers, 8600, Dübendorf, Switzerland

A B S T R A C T

The effect of alumina and carbonates on magnesium silicate hydrate (M-S-H) cements was investigated at high Mg/Si ratios (1.5–2.5), constant Na_2CO_3 concentration (17 g/L) and Al/Si ratio of either 0, 1 or 3.2. Either MgO or MgO/hydromagnesite (50/50 wt %) was used, as well as silica fume, metakaolin or amorphous Al_2O_3. Thermogravimetric analysis (TGA), X-ray diffraction (XRD), ^{29}Si and ^{27}Al MAS NMR data showed that M-(A-)S–H phases formed in all cases and hydrotalcite in presence of aluminum. Little hydromagnesite had reacted in the presence of aluminum. The ^{23}Na MAS NMR data showed that only little sodium was sorbed; the thermogravimetric analysis coupled with infrared exhaust gas analysis and ^{13}C MAS NMR data showed that carbonates were incorporated in the hydrotalcite and traces of carbonate were sorbed. Thermodynamic modelling carried out with an updated Mg-phases database was in relatively good agreement with the phase assemblage observed if the reactivity of the starting materials was considered.

1. Introduction

The cement industry is responsible for approximately 7% of all man-made CO_2 emission [1], and there are urgent needs to decrease these CO_2 emissions. One possible option between the different routes to reduce the CO_2 emissions of cement production is to develop alternative binders. The alkaline activation of calcined clays or other reactive aluminosilicates (AAMs) is one of them [2]. Such binders harden due to the formation of sodium alumino-silicate hydrates (N-A-S-H), which are hydrated zeolitic precursor phases [5–8], providing good compressive strength [3]. AAMs (Alkali-activated' materials) are typically produced using a high pH solution rather than water due to the lower reactivity of the calcined clay compared to PC clinker [4]. These materials can show good mechanical strengths, but are still niche products as they are more challenging to cure, potentially more expensive, and the alkali hydroxide solutions may cause health and environmental issues [5,6]. Recent work looked at MgO as activator to partially or fully replace the expensive and hazardous NaOH activator solutions [7,8]. The production of MgO from burning $MgCO_3$ rocks, however, has currently a high CO_2 footprint, although slightly lower than for the NaOH activator solution [6,9]. In the future, the most viable route to obtain MgO would be the production of MgO from Mg silicate rocks without releasing fossil CO_2 [10,11].

In AAMs, Portland cements (PC) or PC blended with blast furnace slags, magnesium oxide precipitates in the presence of aluminium as hydrotalcite [12–17]. Hydrotalcite phases, magnesium aluminate layered double hydroxides (LDHs), present a variable Mg/Al due to a substitution of Mg^{2+} by Al^{3+} in the brucite-like sheet, which generates positive charges in the structure. The positive charge layer is compensated by anions accompanied by water in the interlayer region [18], with CO_3-hydrotalcite being more stable than OH- and SO_4–hydrotalcite [18–20]. The formation of hydrotalcite positively contributes to compressive strength, as shown by Refs. [17,21]. The authors found that the mechanical properties of AAMs in the presence of additional MgO are improved.

Another potential alternative binder based on magnesium compounds suggested in literature is based on the hydration of blends of reactive silica and magnesia [22]. The interest in magnesium silicate cements grew in the last decades, due to its potential applications as low pH cement for radioactive waste storage and radionuclide retention [22–27]. Magnesium-based cements are based on the direct hydration of reactive magnesia and silicate sources; their hydration results in precipitation of the magnesium silicate hydrate phase (M-S-H) with Mg/Si ratio of about 1 [22]. High compressive strengths of up to 50–80 MPa (on pastes [28] or on concretes [29]) can be reached if activated by sodium hexametaphosphate. In the presence of Na_2CO_3, M-S-H forms faster, and a higher Mg/Si ratio of up to 1.5 can be reached [30], as the formation of aqueous magnesium carbonate complexes destabilise the

---

* Corresponding author. Empa, Swiss Federal Laboratories for Materials Science and Technology, Laboratory for Concrete and Asphalt, 8600, Dübendorf, Switzerland.
E-mail address: ellina.bernard@empa.ch (E. Bernard).

Table 1

Chemical composition of the binder components used (wt. %).

	Metakaolin	MgO	Mg(OH)$_2$	hydromagnesite	Silica fume (low grade)	Silica fume (high grade)
SiO$_2$	54.17	0.5	<0.11	<0.03	96.1	97.34
Al$_2$O$_3$	39.76	0.2	<0.11	<0.03	0.23	<0.11
Fe$_2$O$_3$	0.59	nd	<0.04	0.04	0.06	0.04
Cr$_2$O$_3$	0.004	nd	<0.003		<0.003	0.003
MnO	0.013	nd	<0.004	<0.001	0.028	0.013
TiO$_2$	0.03	nd	<0.019	0.007	<0.019	<0.019
P$_2$O$_5$	0.102	nd	<0.017	0.010	0.117	<0.017
CaO	0.4	1.8	<0.05	0.41	0.3	<0.05
MgO	0.35	96	68.67	42.62	0.38	<0.08
K$_2$O	2.62	nd	<0.03	<0.01	0.79	<0.03
Na$_2$O	0.06	nd	<0.06	0.08	0.17	<0.06
SO$_3$	0.04	nd	0.11	0.06	0.19	<0.04
L.O.I.[a]	1.78	1.5	31.18	56.75	1.57	2.51
total	99.94	100	99.96	99.96	99.94	99.91
Specific surface area (m^3/g) (BET)	13.28	30[b]	90.42[c]	33.35	21.08	200
Amorphous content (wt. %)[d]	82[d]	Not determined	Not determined	Not determined	Not determined	Not determined
Density (g/cm^3)	2.61[e]	3.49[e]	3.31[c&e]	2.04[e]	2.35[e]	2.22[e]

[a] Loss On Ignition.

[b] data given from the producer.

[c] measured on the MgO, i.e. after heat process of the Mg(OH)$_2$.

[d] The amorphous content based on crystalline phases quantified from Rietveld method (quartz ~ 2 wt %, microcline ~12 wt %, illite ~4 wt %) from the XRD pattern. Taking into account the XRF and XRD, the Si/Al ratio in the amorphous phases was estimated to ~1.

[e] measured by pycnometry.

primary formed, metastable brucite [30]. No investigations on the change of Mg/Si ratio in M-S-H are yet available in terms of mechanical performance.

The combination of MgO with reactive aluminosilicates has recently been studied as alternative binder [8,31–35] bridging the chemistries of AAMs containing MgO and M-S-H binders containing reactive aluminate. Clays are widely available in the Earth's crust compared to the availability of silica fume [36,37] and can be calcined to obtain reactive aluminosilicates as alumina and silicate sources [38]. The presence of aluminium has positive effects for MgO-silica binders as the formation of additional hydrotalcite together with M-S-H has been observed in mixes with metakaolin, which lowered the porosity and improved the mechanical properties [34,35]. Similarly to the destabilization of brucite by aqueous magnesium carbonate complexes in Al-free system [30], a faster consumption of brucite is observed with acceleration of M-(A-)S–H and hydrotalcite formation in the MgO-metakaolin system in presence of sodium carbonates [39].

The presence of reactive MgO, silica and alumina might also lead to the formation of magnesium (alumino-)silicate hydrates (M-(A-)S–H) [33,40,41] and/or to the formation of zeolitic phases at high pH [42]. M-(A-)S–H phases are, similar to M-S-H, hydrated nano-crystalline phyllosilicates with variable Mg/Si and Al/Si ratios. The M-(A-)S–H structure consists of mixed layers T:O or T:O:T of silicate [43,44], and alumina can be incorporated in both tetrahedral and octahedral layers [33]. At relatively low pH values (pH 8–10), less aluminate seems to be within the M-S-H structure while more hydrotalcite is formed [41]. The nature and amount of hydrotalcite, zeolite, M-(A-)S–H, brucite and/or magnesium carbonates phases formed depends on the pH values and the availability of aluminate, silicate and carbonate ions [17,30,42,45,46], although the specific conditions governing the precipitation of a particular phase are still unknown. The goal of this study is to provide an in-depth understanding of the effect of aluminates and carbonates on the stability of M-S-H phases, based on an experimental study using advanced characterizations methods and based on thermodynamic

Table 2

Composition of the pastes.

		MS[a]	H-MS[a]	AMS	H-AMS	3AMS	H-3AMS
MgO (g)	Magnesium oxide	*20.0*	*11.7*	14.2	8.6	12.5	7.8
Mg$_5$(CO$_3$)$_4$(OH)$_2$ • 4H$_2$O (g)	Hydromagnesite		*11.7*		8.6		7.7
Al$_2$O$_3$·2SiO$_2$ (g)	Metakaolin			25.8	22.8	13.8	12.3
amorphous AlO(OH) (g)	Amorphous boehmite					13.8	12.2
SiO$_2$ (g)	Silica fume high grade	*7.8*	*6.2*				
SiO$_2$ (g)	Silica fume low grade	*12.2*	*10.4*				
S$_a$ (Na$_2$CO$_3$ = 17 g/L)				40	40	40	40
S$_b$ (Na$_2$CO$_3$ = 8.5 g/L)		*80*	*80*				
Na$_2$CO$_3$ (g)		*0.68*	*0.68*	0.68	0.68	0.68	0.68
Solution/Binder (wt. %)		*2*	*2*	1	1	1	1
Mg (mol)		*0.50*	*0.42*	0.35	0.31	0.31	0.28
Si (mol)		*0.33*	*0.28*	0.23	0.20	0.12	0.11
Al (mol)				0.23	0.20	0.39	0.35
molar Mg/Si		*1.5*	*1.5*	1.5	1.5	2.5	2.5
molar Mg/Al				1.5	1.5	0.8	0.8
molar Al/Si				1.0	1.0	3.2	3.2
molar carbonate/Mg		*0.013*	*0.254*	0.018	0.258	0.021	0.258

[a] studied in detail in [30].

calculations to obtain insights into the factors governing the composition of the hydrated phases and to relate the phase assemblage and reaction degree to the compressive strength.

The phase assemblage and compressive strength of binders consisting of blends of (i) metakaolin or reactive alumina and silica fume with different Al/Si ratios and (ii) magnesium oxide activated by hydromagnesite ($Mg_5(CO_3)_4(OH)_2 \cdot 4H_2O$) and/or sodium carbonate (Na_2CO_3) solution were investigated. A high Mg/Si ratio ≥ 1.5 is used to promote the formation of hydrotalcites and Mg-carbonates in the mixes.

2. Materials and methods

2.1. Raw materials

The chemical compositions of the raw materials (except for Na_2CO_3 and $Al(OH)_3$) are presented in Table 1. MgO was produced either by burning $Mg(OH)_2$ (95% reagent grade) at 600 °C for 2 h in a laboratory furnace or commercially obtained (96 wt% MgO). High grade (purity >98 wt % containing residual HCl [47]) and low grade (purity >96 wt %) silica fume were used as reactive silica sources. Metakaolin and hydromagnesite were commercial products and used for the addition of reactive silica plus alumina and of carbonate. Reactive alumina was made from heating $Al(OH)_3$ (purity >99.5 wt %) at 600 °C during 2 h. The particle size distributions of the different materials as obtained by laser diffraction are given in Figure S 1.

2.2. Design of the experiments

2.2.1. Preparation of pastes

Paste samples were prepared with different Mg/Si (1.5 and 2.5) and Al/Si ratios (1 and 3.2) as summarized in Table 2 and named as AMS (Mg/Si = 1.5, Al/Si = 1) and 3AMS (Mg/Si = 2.5, Al/Si = 3.2). H-AMS and H-3AMS designate samples where half of the MgO was replaced by hydromagnesite. The samples MS and H-MS (Mg/Si = 1.5, Al/Si = 0) from Ref. [30] are used as references for comparison with Al-free samples. Sodium carbonate solutions for the activation were prepared by dissolving 8.5 or 17 g of Na_2CO_3 (Sigma Aldrich, anhydrous, $\geq$99.8%) per litre. The experiments were carried out at 20 °C using a solution/binder ratio (S/b) of 1 for the aluminate containing samples or 2 for the aluminate free samples as detailed in Table 2. The paste samples were mixed by hand during 30 s using a spatula.

Directly after mixing the pastes were cast in 12 mL PE-bottles, sealed and stored at 20 °C. After 3, 7, 28 and 182 days the pastes were crushed, and hydration was stopped by submerging the specimens for 15 min in isopropanol. The solid was filtered, rinsed with diethylether and dried for 15 min at 40 °C [48]. Afterwards the samples were ground by hand in an agate mortar and analysed by TGA and XRD within the next 2 days; the remainders of the samples were stored in desiccators at a relative humidity of ~34% (over saturated $CaCl_2$ solution) until further analyses by NMR.

2.2.2. Preparation of mortars

Flexural and compressive strength were tested on mortar specimens. The mortars were mixed and cured according to EN 196-1 with additional adaptations due to the smaller prism size and longer curing times. Raw materials used for mortar preparation were changed from pure materials to technical materials to ensure that sufficient sample material was available for casting. Thus, 50% of the MgO was replaced by less pure, industrial grade MgO, and the high grade silica fume was entirely replaced by the low grade one (Table 1). Mortars were mixed according to a 3:1 wt% standard sand/binder ratio. A superplasticizer based on polycarboxylate-ether was added (between 1.5 and 3 wt % of the binder referred to the superplasticizer solution as delivered) to achieve proper workability. Water-to-solid ratio (w/s) was adjusted accordingly to the lowest possible water amount for a sufficient workability to cast mortar samples, resulting in water/solid ratio (w/s) = 0.9. After casting the

mortars were demoulded after 24 h and cured in a climate chamber (20 °C and 98% relative humidity) until testing was performed.

2.3. Characterisation techniques

2.3.1. X-ray diffraction analyses

X-ray diffraction analyses (XRD) were performed with a PANalytical X'Pert Pro MPD diffractometer in Bragg-Brentano configuration, equipped with a Cu X-ray source at 45 mV voltage and 40 mA intensity and the X'Celerator detector. The samples were scanned from 5 to 75° 2θ. The Rietveld quantification was carried out with X'pert Highscore Plus software and the method of external standard (G-factor approach) using CaF_2 to quantify the crystalline phases in the samples [49,50].

2.3.2. Thermogravimetric analyses

Thermogravimetric analyses (TGA) were carried out using a Netzsch STA 449 F3 Jupiter TGA apparatus coupled with a Bruker Fourier-transform infrared (FT-IR) spectrometer for the analysis of the exhaust gases. Approximately 40 mg of each sample was heated from 30 to 980 °C with a heating rate of 20 K per minute in 150 μL alumina crucibles. The infrared absorbances of H_2O and CO_2 were integrated in the ranges of 1300–2000 cm^{-1} (O–H bending vibration in H_2O molecules) and 2200–2450 cm^{-1} (C=O stretching vibration) respectively, and used as relative measures of H_2O and CO_2 contents in the exhaust gases as detailed in Ref. [20].

2.3.3. ^{29}Si MAS NMR

The ^{29}Si MAS NMR single pulse experiments were conducted on Bruker Avance III 400 NMR spectrometer (Bruker BioSpin AG, Fällanden, Switzerland) using a 7 mm CP/MAS probe at 79.5 MHz applying the following parameters: 4500 Hz sample rotation rate, 7168 scans, 30° ^{29}Si pulse of 2.5 μs, 30 s recycle time, RF field strength of 33.3 kHz during SPINAL64 proton decoupling. The ^{29}Si NMR chemical shifts were referenced to the most intense resonance at −2.3 ppm of an external sample of an octamethylsilsesquioxane (Aldrich No. 52,683-5) which was referenced to tetramethylsilane (TMS, δ^{29}Si = 0.0 ppm), details are given in Ref. [41]. For representative samples, ^{29}Si T_1 relaxation times were evaluated by saturation recovery NMR experiments. For samples containing M-S-H phases (samples "pure M-S-H″ and "MS" from Ref. [30]) relaxation times from 60 to 80 s were determined for the three narrow main resonances at −79, −86 and −92 ppm. For the sample containing aluminium "AMS", T_1 values in the order of 5 s were evaluated, indicating that the relative amounts of M-S-H phase determined by the ^{29}Si MAS NMR line shape analysis of the Q^n sites in the case of the samples containing Al were quantitative.

The observed ^{29}Si NMR resonances were assigned using the Q^n classification, where one Si tetrahedron is connected to n Si tetrahedra, where n varies from 0 to 4. The lineshapes of the experimental data were analysed by non-linear least-square fits using the "DMFIT" software developed by Massiot et al. [51]. The presence of unreacted silica was confirmed by the resonance Q^4 at −110 ppm while the presence of metakaolin was confirmed by the resonances at ~105 ppm. Reliable lineshape analysis of the metakaolin was possible with the application of signals Q^A and Q^B at −98.3 and −108.5 ppm with a ratio between 3 and 4. The spectra associated to the aluminium containing samples presented mixed broad signals between −76 and −115 ppm. The line shape analysis of the M-A-S-H phases indicated the presence of Q^2(Al) and Q^3(Al) at −81 to −82 ppm and −90 to −91 ppm respectively [33,41]. To avoid overinterpretation of the spectra, we have chosen to carry out the deconvolution with a minimal number of signals (only Q^1, Q^2, and Q^3 of the M-S-H), although the width of the signals appeared bigger than for the aluminium free samples potentially indicating the presence of Q^2(Al) and Q^3(Al).

The ^{29}Si CP-MAS NMR spectra were recorded using the following parameters: 7.5 μs 90° excitation pulse on ^1H channel, 0.2, 0.5, 1, 2, 3, 4 and 5 ms contact times (28.7 kHz spinlock field on ^{29}Si channel)

applying ramps from 100 to 50% of power level on the proton channel, 4500 Hz MAS rates, 3 s relaxation delays, the above mentioned proton decoupling conditions and 6142 up to 8192 scans were recorded to yield reasonable signal-to-noise ratios. To compare the CP MAS NMR data within each series of spectra, the signal intensities of the 6 data sets recorded with 0.2 ms contact time were each set to the value 100 and then the intensities of each spectra were normalized by the absolute signal intensities (the weight of each sample and the number of scans), considering the total intensity of the MS sample, 0.2 ms contact time = 100%.

2.3.4. ^{27}Al MAS NMR

The ^{27}Al NMR spectra were measured using a 2.5 mm CP/MAS probe on the same instrument as described above. The ^{27}Al MAS NMR single pulse experiments were recorded at 104.3 MHz applying the following parameters: 25′000 Hz sample rotation rate, 3072 scans, $\pi/12$ pulses of 1.0 μs, 1.0 s recycle delays ensuring quantitative recording of the data no ^{1}H decoupling applied during the acquisition. The ^{27}Al NMR chemical shifts were referenced to an external sample of Al(acac)$_3$, which in turn was calibrated to the signal from a solution of 1.1 m Al(NO$_3$)$_3$ in D$_2$O at 0.0 ppm. All absolute signal intensities of individual samples were evaluated from the absolute intensities over the full spectral range determined by the Bruker TopSpin software with respect to the signal intensity of sample 3AMS and by the sample weights (all ^{27}Al NMR spectra recorded with exactly the same NMR parameters). The individual ^{27}Al MAS NMR spectra were analysed by the line shape fitting software "DMFIT" [51]. Generally, the fitting of the octahedral sites was performed using i) a Lorentzian shape at 9 ppm (FWHM of 4–5 ppm) and ii) a quadrupolar broadened shape using the "Czjzek simple" [52] model starting with the parameters FWHM CS = 10 ppm (full width at half maximum of the isotropic chemical shift Gaussian distribution), CQ = 5.3 MHz (peak value of the quadrupolar coupling of the Czjzek/GIM distribution) and d = 5 (exponent of the Czjzek distribution). The signals for the petahedral and tetrahedral Al sites were fitted as well with the "Czjzek simple" model (FWHM CS = 12 ppm, CQ ∼ 4–5.5 MHz and d = 5) [41].

2.3.5. ^{13}C MAS NMR

Solid-state ^{13}C CP-MAS NMR spectra were recorded using a 7 mm CP-MAS probe. Weighed amounts of material (140–230 mg) were thoroughly packed into 7 mm zirconia rotors and to allow smoother sample rotation Teflon inserts (3 mm thickness) were used. The filling heights were carefully chosen so that the Teflon spacer was in direct contact with the cap ensuring equivalent sample volumes for each rotor. The ^{13}C CP-MAS NMR spectra were recorded at 100.6 MHz, using the following parameters: 6.0 μs 90° excitation pulse on ^{1}H channel, 2 ms contact time (32.8 kHz spin lock field on ^{13}C channel) applying ramps from 100 to 50% of power level on the proton channel (spin lock field of 43 to 22 kHz), rotations rates of 4000 Hz, 5 s repetition time, 41 kHz SPINAL 64 proton decoupling was applied during acquisition and appropriate numbers of scans (3072 up to 20480) were recorded to yield reasonable signal-to-noise ratios. All absolute signal intensities of the individual samples were normalized by weight and by the number of scans with respect to the ^{13}C CP MAS NMR spectrum of a sample containing pure hydromagnesite starting material (see section 3.4). The lineshapes of the experimental data were analysed by non-linear least-square fits using the "DMFIT" software developed by Massiot et al. [51].

The individual spectra were analysed by line shape simulations applying i) Lorentzian shapes for the two resonances of hydromagnesite at 165.6 (resonance A) and 163.4 (resonance B) ppm (line widths of 80–100 Hz) as detailed in Ref. [53], respectively and ii) one (aluminium free samples) or two additional Gaussian shapes (line widths of 350–800 Hz) for the much broader signals at 170.0 and 167.1 ppm were needed to simulate the signal intensity in the foot of the narrow resonances.

From the relative proportions of the resonances of hydromagnesite in the individual ^{13}C CP MAS NMR spectra and the absolute signal intensities (see above), the contents of hydromagnesite were determined. Please note that for the hydromagnesite NMR resonances observed at 165.6 and 163.4 ppm T$_1$ relaxation times in the order of 140–170 s were obtained by a saturation transfer experiment. This, of course, makes it impossible to record quantitative single pulse ^{13}C MAS NMR data for series of samples. Assuming that the relaxation time and polarization transfer rates of this compound do not vary significantly from sample to sample, we therefore chose the indirect route via CP MAS NMR experiments for the quantification of hydromagnesite.

2.3.6. ^{23}Na MAS NMR

The ^{23}Na MAS NMR data was recorded at 105.9 MHz on a 4 mm CP/MAS probe applying the following parameters: 13′000 Hz sample rotation, 1024 scans, 20° pulses of 2.0 μs, 1 s recycle delays, no ^{1}H decoupling during acquisition. The ^{23}Na NMR chemical shifts were externally referenced to a 0.1 M solution of NaCl in D$_2$O [54]. The lineshapes were analysed by applying Lorentzian lineshapes [51]. Please note that the ^{23}Na MAS NMR resonances throughout were symmetrical and lineshapes could be simulated by using Lorentzian shapes. All attempts to fit the ^{23}Na NMR data with 2nd order quadrupolar broadened lineshapes failed, which means that the sodium cations must be quite mobile in the observed phases. The ^{23}Na MAS NMR data were recorded for the 6-month-old samples only. All absolute signal intensities of individual samples were evaluated from the absolute intensities over the full spectral range determined by the Bruker TopSpin software with respect to the signal intensity of the 3AMS sample and normalized by the weight of the samples (all the other parameter for the recording of the spectra were identical).

2.3.7. pH measurements

The pH values of the pore solutions of the aged samples were estimated based on leaching test following the procedure outlined in Plusquellec et al. [55] and Alonso et al. [56]. Such simple leaching tests give directly reliable pH values for "low-pH" cements (pH < 12, see [56]) as studied here, although the pH measurement obtained from the leaching test can be slightly (<0.2 log units) lower than the measurement of pressed out pore solution [56]. In contrast to low pH cements, the pore solutions of cements with high alkali concentrations would need to be corrected for the dilution of solution by the leaching as detailed in Ref. [55]. 1.5 g of hydrated cement powder was blended with 1 or 1.5 g of distilled water and equilibrated for 15 min, 3 h and 24 h prior to measurement. The data measured after the different times and for different water additions agreed within 0.1–0.2 pH unit and the average of the 6 values is given in the following. The pH measurements were carried in the supernatant of the suspension at 23 °C using a Thermo Scientific™ Orion™ PerpHecT™ ROSS™ Combination pH Micro Electrode.

2.3.8. Compressive and flexural strength

Flexural and compressive strength were tested on 100 × 25 × 25 mm^3 mortar specimen. The mortars were tested according to EN 196-1 with additional adaptations due to the smaller prism size and longer curing times. Mortars were demoulded 24 h after casting and cured in a climate chamber (98% relative humidity) until testing was performed. Compressive and flexural strength were measured with a hydraulic press after 3 days (1 prism), 7 days (2 prisms), 14 days (2 prisms), 28 days (3 prisms), and 91 days (2 prisms). Flexural strength data was acquired from destructive bending experiments (applied force per time: 0.02 kN/s) resulting in two prism halves per specimen. Compressive strength was measured on prism halves applying a pressure load of 0.5 MPa/s.

2.4. Thermodynamic modelling

Thermodynamic modelling was carried out using the Gibbs free energy minimization program GEMS [57,58]. GEMS software is a broad-purpose geochemical modelling code, which computes

Table 3

Standard thermodynamic properties (25 °C) and molar volumes of the phases relevant to the studied systems.

	$\log K_{S0}$	$\Delta_f G°$ (Gibbs free energy of formation)	$S°$	$Cp°$	$V°$ (molar volume)	Ref.
		[kJ/mol]	[J/mol/K]	[J/mol/K]	[cm^3/mol]	
Brucite, $Mg(OH)_2$	−11.16	−832.2	63.1	77.3	24.6	[59,62]
Microcryst. $Al(OH)_3$	−0.67	−1148.4	140	93.1	32.0	[63]
H_2O (zeolitic water)		−237.2	69.9	75.4	18.1	[60,62]
CO_3-hydrotalcite, Mg/Al = 2 $Mg_4Al_2(OH)_{12}(CO_3)\cdot4H_2O$	−53.0	−6828.0	621	727	22.2	[20]
CO_3-hydrotalcite, Mg/Al = 3 $Mg_6Al_2(OH)_{16}(CO_3)\cdot5H_2O$	−75.3	−8729.5	810	953	30.1	[20]
CO_3-hydrotalcite, Mg/Al = 4 $Mg_8Al_2(OH)_{20}(CO_3)\cdot6H_2O$	−97.6	−10631.0	1022	1200	38.0	[20]
OH-hydrotalcite, Mg/Al = 2 $Mg_4Al_2(OH)_{13.8}(CO_3)_{0.1}\cdot4H_2O$	−49.9	−6618.16	619	723	22.4	[20]
OH-hydrotalcite, Mg/Al = 3 $Mg_6Al_2(OH)_{17.8}(CO_3)_{0.1}\cdot5H_2O$	−72.2	−85196.8	815	959	30.3	[20]
OH-hydrotalcite, Mg/Al = 4 $Mg_8Al_2(OH)_{21.8}(CO_3)_{0.1}\cdot6H_2O$	−94.5	−10421.2	1029	1209	38.2	[20]
M-S-H, Mg/Si = 0.75 $(MgO)_{0.75}(SiO_2)_1(H_2O)_{1.75}$	−14.4	−1609.2	135	159	47.5	Adapted from [43]
M-S-H, Mg/Si = 1.5 $(MgO)_{1.5}(SiO_2)_1(H_2O)_{2.5}$	−23.57	−2355.7	216	250	74.0	[43]
M-A-S-H, Mg/Si = 0.75 $(MgO)_{0.75}(Al_2O_3)_{0.1}(SiO_2)_1(H_2O)_{1.5}$	−15 ± 2	−1985.2				Estimated in [33]
M-A-S-H, Mg/Si = 1.5 $(MgO)_{1.5}(Al_2O_3)_{0.1}(SiO_2)_1(H_2O)_{1.8}$	−24 ± 2	−2684.1				Estimated in [33]
Analcime, $Na_2Al_4Si_4O_{12}\cdot2H_2O$	−26.8 ± 0.8	−6139.7	469	425	194.8	[61]
Low-silica P–Na, $Na_2Al_2Si_2O_8\cdot3.8H_2O$	−19.6 ± 0.6	−4858.7	374	384	153.5	[61]
Phillipsite–Na, $Na_{2.5}Al_{2.5}Si_{5.5}O_{16}\cdot5H_2O$	−39.4 ± 1.2	−8717.8	692	620	304.7	[61]
Linda type A (LTA), $Na_{1.98}Al_{1.98}Si_{2.02}O_8\cdot5.31H_2O$	−18.2 ± 0.6	−5203.8	584	513	187.0	[61]
zeolite 4 Å, $Na_2Al_2Si_2O_8\cdot4.5H_2O$	−20.5 ± 0.6	−5029.9	536	475	187.0	[61]
Sodalite–Na, $Na_8Al_6Si_6O_{24}(OH)_2\cdot2H_2O)$	−65.2 ± 2.0	−13221.4	943	895	424.7	[61]
chabazite–Na, $Na_2Al_2Si_4O_{12}\cdot6H_2O$	−31.9 ± 1.0	−7117.6	548	578	250.0	[61]
Faujasite–X, $Na_2Al_2Si_{2.5}O_9\cdot6.2H_2O$	−21.9 ± 0.7	−5857.8	566	586	195.8	[61]
Faujasite –Y, $Na_2Al_2Si_4O_{12}\cdot8H_2O$	−29.5 ± 0.9	−7578.2	734	739	282.9	[61]
Natrolite, $Na_2Al_2Si_3O_{10}\cdot2H_2O$	−26.6 ± 0.8	−5305.2	360	359	169.4	[61]
Mordernite–Na, $Na_{0.72}Al_{0.72}Si_{5.28}O_{12}\cdot2.71H_2O$	−22.5 ± 0.7	−5956.0	388	405	210.6	[61]
Magnesite, $MgCO_3$	−8.29	−1029.3	65.7	75.9	28.0	[59]
Nesquehonite, $MgCO_3\cdot3H_2O$	−5.27	−1723.6	180.5	237.8	74.8	[62,64]
Lansfordite $MgCO_3\cdot5H_2O$	−5.24	−2197.8	249.5	317.8	103.2	[65,66]
Hydromagnesite, $Mg_5(CO_3)_4(OH)_2\cdot4H_2O$	−37.08	−5856.8	478.7	526.6	208.8	[67–69]
Dypingite, $Mg_5(CO_3)_4(OH)_2\cdot5H_2O$	−34.94	−6081.7	522.8	566.6	225.9	[62,64,70]
Artinite, $Mg_2(CO_3)_1(OH)_2\cdot2H_2O$	−18.67	−2568.6	232.9	296.1	96.9	[67,68]

equilibrium phase assemblage and speciation in a complex chemical system from its total bulk elemental composition. The thermodynamic data for aqueous species as well as for SiO_2 and brucite were taken from the PSI-Nagra and the CEMDATA18 thermodynamic databases [59,60]. The data for M-A-S-H, zeolites and hydrotalcite were taken from Refs. [20,33,61], respectively. The updated dataset for Mg-carbonate phases given in Ref. [30] was also included in the calculations. A summary of the data relevant to the studied systems is given in Table 3.

The samples containing metakaolin showed a partial reaction, therefore, the thermodynamic modelling was adapted with the reacted metakaolin estimated with ^{29}Si MAS NMR data.

3. Results

3.1. TGA and XRD

3.1.1. Al_2O_3–MgO–SiO_2 system

The effect of aluminium was studied in two series (AMS and 3AMS and compared to the Al-free MS series detailed in Ref. [30]. The AMS series had an Al/Si molar ratio = 1 using metakaolin, while the 3AMS series contained more aluminium due to the combination metakaolin and amorphous alumina (Al/Si = 3.2) (Table 2).

X-ray diffraction patterns of AMS pastes hydrated up to 182 days are compared to the non-hydrated mix in Fig. 1a. In the diffraction pattern obtained for the unhydrated AMS, the reflections observed are attributed to MgO (37.1, 42.9, 62.2, 74.6 °2θ CuKα) along with small traces of quartz, K-feldspar (microcline) and illite, which were present in raw metakaolin. During hydration, the relative intensity of the reflections corresponding to MgO decrease with time (until ~2 wt % after 182 days), while broad reflections at ~11, ~23, ~35, ~39, ~47, ~60 °2θ CuKα, characteristic for hydrotalcite [71], are observed at each hydration time. In contrast, in the absence of aluminium (MS hydrated pastes [30], Fig. 1c) brucite, $Mg(OH)_2$, is formed as an intermediate phase as well as in the absence of bicarbonate (MgO–SiO_2–$NaAlO_2$ system [41, 42]). This could indicate that the joint presence of alumina and carbonate slows down the MgO dissolution, or prevents brucite formation and/or leads to the fast precipitation of other Mg-containing solids such as hydrotalcite. Actually, another study showed that brucite and MgO
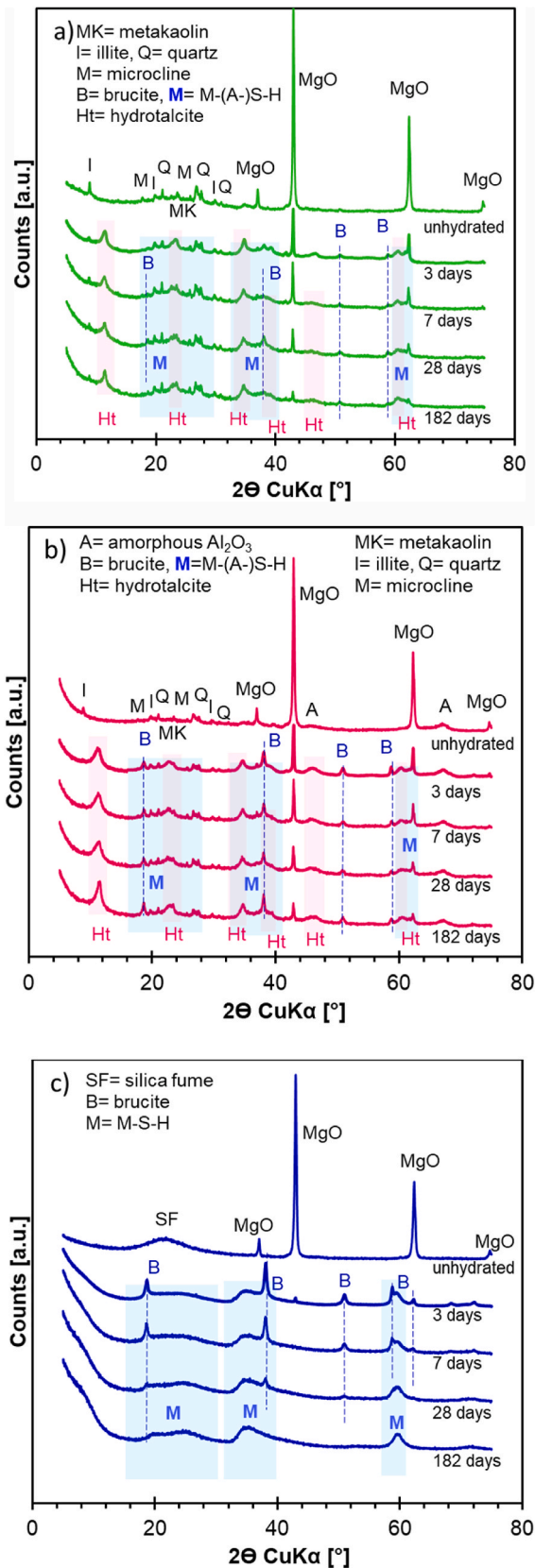
Fig. 1. X-ray diffraction (XRD) patterns of a) AMS pastes, b) 3AMS pastes and c) MS pastes (adapted from Ref. [30]) after different hydration times. Light blue areas correspond to the regions of the broad M-S-H reflections, and light pink areas to the regions of the reflections related to hydrotalcite. (For interpretation of the references to colour in this figure legend, the reader is referred to the Web version of this article.)
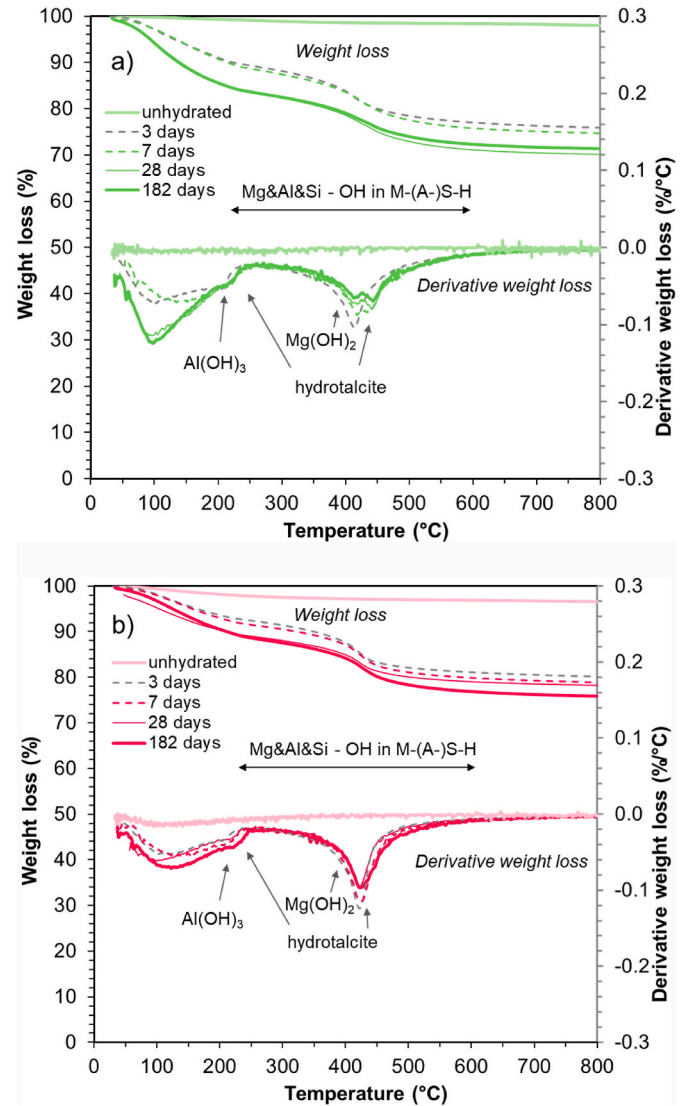

Fig. 2. Thermogravimetric analysis (TGA) of a) AMS pastes and b) 3AMS pastes after different hydration times.

are present in lower quantity in presence of sodium carbonates in the AMS system [39]. This indicates that sodium carbonates destabilise the MgO and brucite as in the MS system [30]. But compared to the MS, the presence of alumina and/or the lower amount of silicate slow down the dissolution of MgO.

The X-ray diffraction patterns of the hydrated 3AMS pastes (Fig. 1b) showed a similar behaviour as the AMS pastes. Over time, MgO reacts and hydrotalcite forms while no or only very little brucite occurs. MgO was quantified at about ~1 wt % after 182 days. The hydrotalcite content in the 3AMS samples appeared to be higher or more crystalline than in the AMS samples; this was attributed to the higher content of aluminium in the 3AMS starting material. However, the relatively poor crystallinity and variable Mg/Al ratios of hydrotalcite-like phases [13, 17] biased its quantification and the estimation of the Mg/Al ratios from XRD data. Finally, broad humps were observed at 20, 27, 35, and 60 °2θ CuKα, indicating tentatively the presence of M-(A-)S–H; however, they were not clearly evidenced by XRD due to their nano-crystalline nature [33]. The presence of AlO(OH) [72] can also be observed in the 3AMS samples indicating little reaction of the raw material added.

TG analyses of the AMS and 3AMS pastes (Fig. 2) confirmed the presence of hydrotalcite in both samples by two distinct water loss regions at ~230 °C and ~420 °C indicating a water and a water/carbonate
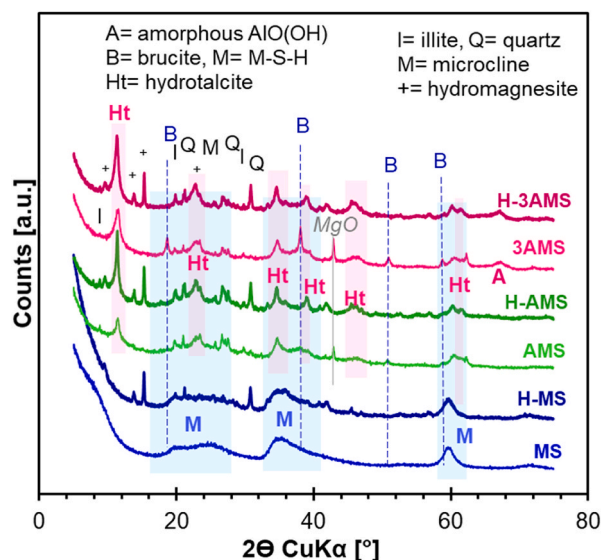
Fig. 3. X-ray diffraction (XRD) patterns of the H-samples (thick plain lines) and the hydromagnesite-free pastes (thin lighter lines) after 182 days. Light blue areas correspond to the regions of the M-S-H broad reflections, light pink to the regions of the reflections related to hydrotalcite. (For interpretation of the references to colour in this figure legend, the reader is referred to the Web version of this article.)

loss, respectively [20,73]. The shoulder observable in the DTG at 220 °C might be related to the presence of nanocrystalline AlO(OH)/Al(OH)$_3$; the weight losses characteristic of poorly crystalline AlO(OH)/Al(OH)$_3$ and hydrotalcite overlap in the region around 200–250 °C (see Fig. S 2) and were thus difficult to interpret. The small amounts of brucite suspected from the XRD data of AMS and 3AMS samples, probably contributed to the 2nd weight loss (at 400–450 °C) mainly assigned to hydrotalcite. Note that in the AMS samples, two weight losses at 400–450 °C can be distinguished while they merged for the 3AMS samples.

The water loss at ~100–120 °C in the TGA data indicated some loosely bound water in the samples, as characteristic for M-(A-)S–H [33] or N-A-S-H phases [74]. After 7 days of hydration, the first water loss between 30 and 200 °C amounts to 7 and 9 wt % in the AMS and 3AMS pastes, respectively. For the 182 days old samples, these values increased to 10 and 14 wt %, respectively, indicating a more significant amount of loosely bound water, i.e. more hydrated phases formed, potentially M-(A-)S–H. The second weight loss between 250 °C and 700 °C characteristic of Mg–OH and Si–OH was also observed in the TG data of the AMS and 3AMS pastes, although less clearly than for pure M-(A-)S–H [33]. This could be due to a lower content of M-(A-)S–H phases in the solid composition.

3.1.2. Effect of hydromagnesite in the Al$_2$O$_3$–MgO–SiO$_2$ system

Half of the MgO was replaced by hydromagnesite to prepare H-AMS and H-3AMS samples (Table 2). The full XRD and TGA data are presented in Fig. S4 and Fig. S5, respectively. Figs. 3 and 4 display XRD and TGA data for the comparison of the hydromagnesite-containing samples with the hydromagnesite-free samples after 182 days. No XRD reflections characteristic of MgO were observed in the H-AMS and H-3AMS samples. This indicated that MgO is already completely dissolved within 7 days (Fig. S4), when added in a smaller quantity (half of the amount than in AMS and 3AMS). Little hydromagnesite reaction was observed in all three H-samples; the characteristic primary reflections at 15.27 and 30.81 °2θ CuKα (Fig. 3) remain well visible. Brucite was present after 7 and 28 days, while it was no more detectable by XRD after 182 days (Fig. S4). The broad hump characteristic of amorphous metakaolin was visible in the samples, and the reflections assigned to
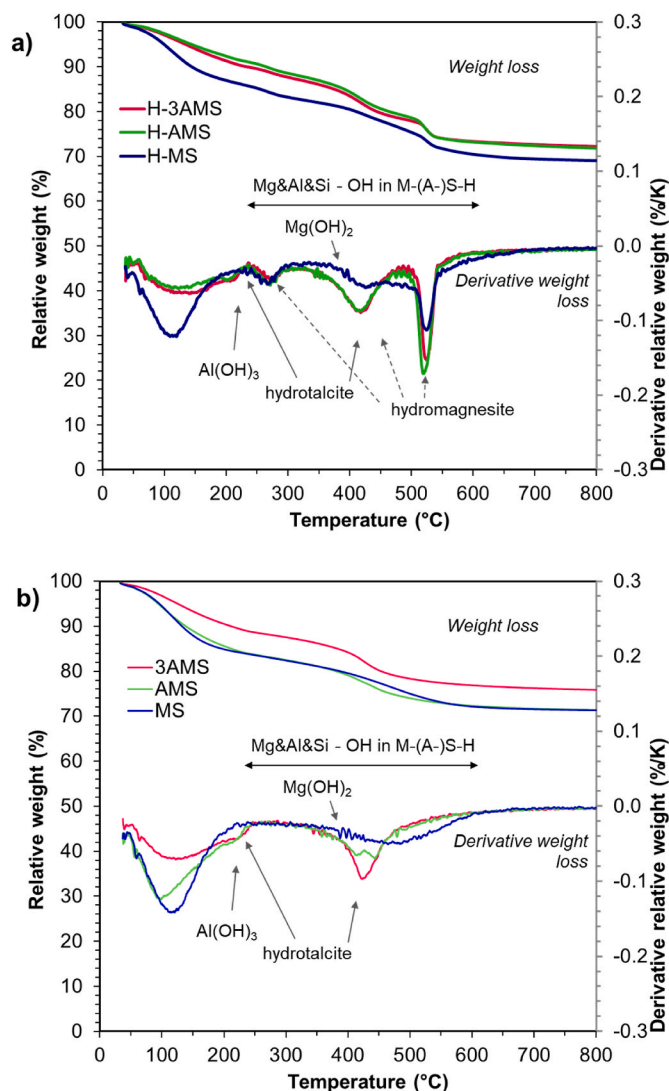
Fig. 4. Thermogravimetric analysis (TGA) of the a) H-sample pastes compared to the b) hydromagnesite-free pastes after 182 days.

hydrotalcite become more evident with increasing hydration time. Finally, the hydrotalcite formed in the H-samples was more visible, this may indicate either more crystalline hydrotalcite or hydrotalcite in larger quantity.

The TGA data of the H-AMS and H-3AMS samples recorded at 182 days are compared to the H-MS, MS, AMS and 3AMS samples in Fig. 4. The data showed the presence of physically bound water (30–200 °C). The weight losses at ~270 °C and ~520 °C were attributable to hydromagnesite. The weight loss at 400–450 °C was attributed to the loss of the hydroxyl groups from brucite with a rather small contribution from the hydromagnesite (Fig. S2), as discussed in Ref. [30] for the Al free samples as displayed in Fig. S5c. In presence of Al, the hydrotalcite also contributed to this weight loss as well observed for the 3AMS sample (Fig. 2b). With increasing hydration time (Fig. S5), this weight loss (~400 °C) decreased indicating less brucite, hydromagnesite or hydrotalcite and shifted to a slightly higher temperature (~410 °C), which was either due to less brucite or hydromagnesite and/or higher crystallinity of the hydromagnesite/hydrotalcite, most likely a combination of a decrease of brucite and a higher crystallinity of the hydrotalcite phases, as observed by XRD (Fig. 3). For the 182-day-old samples, an additional weight loss around 220 °C appeared, associated with more hydrotalcite or the possible occurrence of Al(OH)$_3$. Similarly to the discussion above, the presence of physical bound water below 200 °C
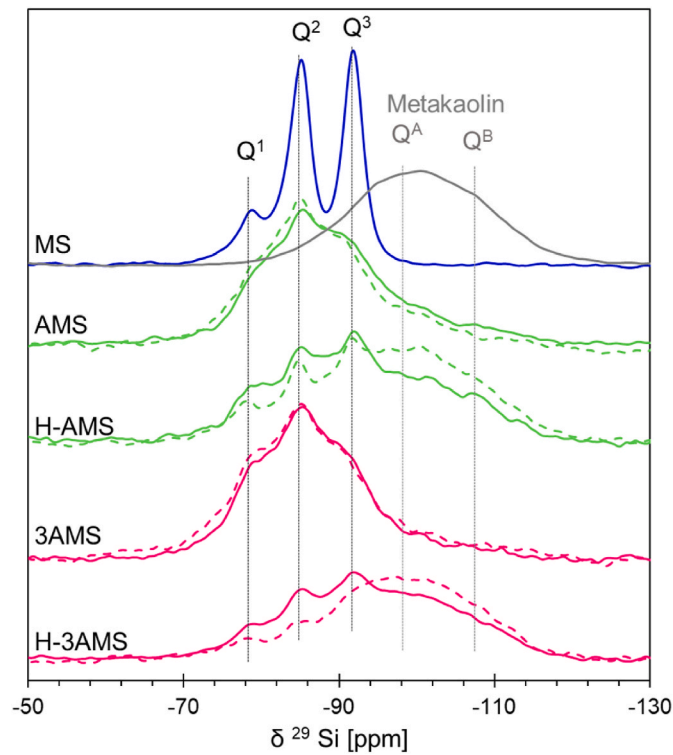
Fig. 5. ^{29}Si MAS NMR spectra of AMS, H-AMS, 3AMS and H-3AMS samples (dashed lines = 28, plain lines = 182 days of hydration). Additional spectra of the MS sample (182 days) and the metakaolin starting material are shown at top.

can be related to M-(A-)S–H phases. It seemed that the total of this physical bound water, and thus of M-(A-)S–H was lower in the presence of alumina than in alumina-free samples (Fig. S5 c.).

3.2. ^{29}Si MAS NMR and H–Si CP MAS NMR data

^{29}Si MAS NMR spectra of AMS, 3AMS, H-AMS and H-3AMS samples are presented in Fig. 5 together with the spectra of the metakaolin used and the MS sample (from Ref. [30]) as references. Numerical results obtained from lineshape analysis of the spectra and the quantification of metakaolin are summarized in Table 4, and examples of the simulated NMR spectra are shown in the SI (Fig. S6 & S7). Reliable lineshape analysis of the metakaolin starting material was possible with the application of two signals only, one at −98.3 ppm (Q^A) and one at −108.5 ppm (Q^B) characteristic of Q^4 signals (see Fig. S6, SI), accounting for a total of 100% of the silicon, with a Q^A/Q^B signal ratio of ~3.8. For line shape simulations to determine the amount of unreacted metakaolin in hydrated samples, the chemical shifts and line widths of the ^{29}Si NMR Q^A and Q^B were varied only slightly; as both resonances are broad, the ratio of Q^A/Q^B was kept within ~3.7 ± 0.2.

In the AMS and 3AMS samples, most metakaolin had reacted within 28 days, with 19 and 14 wt % of the silicate attributed to remaining metakaolin, respectively. After 182 days, 19 and 9 wt % of unreacted metakaolin were found, indicating a slow further reaction of metakaolin in the 3AMS sample. In contrast, the H-AMS and H-3AMS samples containing hydromagnesite as reactant in the original samples still maintain high levels of metakaolin after hydration: 63 and 78% after 28 days and 47 and 58% after 182 days, respectively (Table 4).

The additional resonances in the spectra were simulated with three signals of Q^1 at −78.7 ± 0.5 ppm, Q^2 at −84.9 ± 0.3 ppm and Q^3 at −91.1 ± 1.0 ppm attributed to resonances of M-S-H [23,43], of M-(A-)S–H [33,41] or of M-S-H in the presence of carbonates [30]. However, the relative amounts of Q^1 were higher ($Q^1/Q^2 \geq 0.6$) than in classical M-S-H ($Q^1/Q^2 \sim 0.3$) and the resonances much broader. Both can be related to the presence of Al in the silica network, for which the presence

Table 4
Assignments of ^{29}Si NMR chemical shifts and relative amounts of Q^n silicon species obtained by simulation of the ^{29}Si MAS NMR spectra shown in Fig. 5 (examples of deconvolutions shown in Fig. S 7).

M-(A-)S–H		Q^1		Q^2		Q^3		Q^1/Q^2	Q^2/Q^3	metakaolin				Total MK	Q^A/Q^B
		δ_{iso}	Rel. amount	δ_{iso}	Rel. amount	δ_{iso}	Rel. amount			Q^A		Q^B			
										δ_{iso}	Rel. amount	δ_{iso}	Rel. amount		
		[ppm]	[%]	[ppm]	[%]	[ppm]	[%]			[ppm]	[%]	[ppm]	[%]	[wt. %]	
MK										−98.3	79.0	−108.5	21.0	100	
MS [30]	182 days	−78.4	11	−85.1	46[a]	−91.8	43	0.3	1.1						
H-MS [30]	182 days	−78.9	10	−85.3	39[a]	−92.0	44	0.4	0.8	−95.6	7				
AMS	28 days	−79.1	23	−84.9	32	−90.6	26	0.7	1.2	−98.3	15	−108.5	4	19	3.8
	182 days	−79.1	21	−85.0	32	−90.8	28	0.7	1.1	−98.3	15	−108.5	4	19	3.8
3AMS	28 days	−78.9	30	−85.0	31	−90.6	25	1.0	1.2	−98.3	11	−108.5	3	14	3.7
	182 days	−79.0	28	−84.8	33	−90.7	30	0.8	1.1	−98.3	7	−108.5	2	9	3.5
H-AMS	28 days	−78.3	11	−84.5	13	−91.0	13	0.8	1.0	−98.3	50	−108.5	13	63	3.8
	182 days	−78.5	13	−85.2	22	−91.7	18	0.6	1.2	−98.3	37	−108.5	10	47	3.7
H-3AMS	28 days	−78.2	7	−84.7	8	−92.1	7	0.9	1.1	−98.3	62	−108.5	16	78	3.9
	182 days	−78.5	10	−85.0	17	−91.5	15	0.6	1.1	−98.3	46	−108.5	12	58	3.8

[a] Q^2(Na) is included in this value.
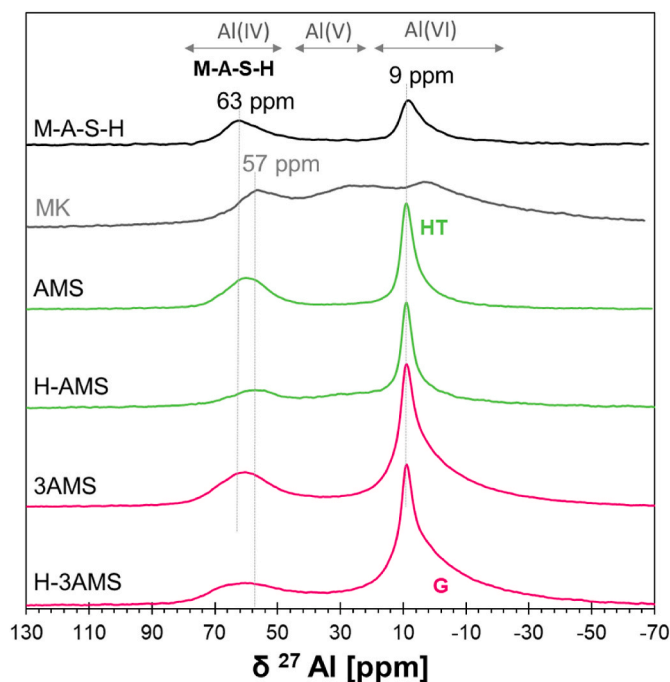
Fig. 6. ^{27}Al MAS NMR spectra of AMS, H-AMS, 3AMS and H-3AMS pastes (182 days) and the reference materials as pure M-A-S-H phase (Mg/Si=1.1, Al/Si=0.15; [33]) and metakaolin starting material. The centers of gravity of specific regions are highlighted by dotted lines and assigned as follows: the signal at 63 ppm to Al(IV)b in M-A-S-H, 57 ppm to Al(IV) in the raw material and the Al(VI)a and Al(VI)b sites at 9–11 ppm to both, M-A-S-H and poorly crystalline hydrotalcite/Al(OH)$_3$. Please note that mean isotropic ^{27}Al NMR chemical shifts of 68 and 56 ppm were determined for the 2 Al(IV) species. For the samples from this study, the relative signal intensity has been corrected for the weight of the samples and the absolute signal intensity with respect to the data of sample 3AMS; HT = symmetric Al(VI) signal attributed to hydrotalcite, G = asymmetric Al(VI) signal attributed to the amorphous Al(OH)$_3$ (see relative amount of Al species given in Table 5).

of Q^2(Al) at approx. −81 ppm and Q^3(Al) at approx. −90 ppm would be expected. However, due to the complexity of the spectra and to the presence of broadened and partially over lapping resonances in the ^{29}Si MAS NMR spectra, the line shape analysis was carried out with a minimum number of signals. Note that the presence of N-A-S-H phases would result in a broadening of the Q^3 and Q^4 signals [75,76], which

could overestimate the content of MK and the M-(A-)S–H in the samples.

The ^{1}H–^{29}Si CP MAS-NMR (cross-polarization magic angle spinning NMR) data have been recorded with varying contact times between 0.2 and 5 ms for the 6 samples after 182 days (Fig. S8).

The variation of the contact time in ^{1}H–^{29}Si CP MAS-NMR experiments permits to probe whether protons of hydroxide groups or water molecules are in the vicinity of tetrahedral silicate. A proton as a hydroxyl group directly bound to silicon will result in a short contact time, while water adsorbed on the surface results in the local maxima reached at longer contact time.

The ^{1}H–^{29}Si CP MAS-NMR data obtained for the MS and H-MS samples from Ref. [30] (Fig. S8a and b) were very similar to the pure M-S-H from Ref. [77] with a maximum reached for Q^1 and Q^2 for a contact time between 1 and 3 ms while Q^3 continued to grow [43,77]. This indicated that the hydroxyl groups must be in the vicinity of Q^1 and Q^2, while none are close to all Q^3 as expected based on the structure of M-S-H [43,77]. A similar behaviour was observed for all aluminium containing samples (Fig. S 8c-f): local CP transfer maxima observed at ca. 1 ms (Q^1) and 2 ms (Q^2) indicated hydroxyl groups in the close proximity to silicate and the ongoing increase of Q^3 intensity over the whole range of contact time (0.2–5 ms). The maximum reached for Q^1 and Q^2 indicated that hydroxyl groups were close to silicate comparable to M-S-H, and the minor Q^3 increase possibly indicated more hydroxyl groups closer to silicate layers (Q^3). This could result from the Si substitution by Al in the tetrahedral layers. Finally, the total amount of the signals is much lower than in the Al-free samples, certainly related to a lower content of M-(A-)S–H phases.

3.3. ^{27}Al MAS NMR data

The ^{27}Al MAS NMR spectra of the AMS, H-AMS, 3AMS and H-3AMS samples (182 days) are shown in Fig. 6, together with data of reference samples of pure M-A-S-H 1.1 0.15 [33] and of metakaolin starting material.

The broad resonances in the ^{27}Al-MAS NMR spectrum of metakaolin underline its amorphous nature. The signals can be assigned to Al(IV), Al(V) and Al(VI) species and from line shape simulations relative amounts of 36, 53 and 11% are determined, respectively (Table 5). The line shape analyses of all samples investigated in this study were performed similarly to those described in detail in Ref. [41], applying two asymmetric Al(IV), one asymmetric Al(V), one asymmetric Al(VI) and one symmetric Al(VI) environments (examples of deconvoluted spectra are given in Fig. S9). The ^{27}Al MAS NMR spectrum of the pure synthetic M-A-S-H showed the presence of large quantities (60%) of Al(VI)a and Al(VI)b at

Table 5
Composition and isotropic ^{27}Al NMR chemical shifts assigned to Al(IV), Al(V) and Al(VI) sites obtained by deconvolutions of the ^{27}Al MAS NMR spectra of the AMS, 3AMS, H-AMS and H-3AMS pastes and of reference materials (^{27}Al NMR spectra shown in Fig. 6, examples of deconvoluted spectra shown in Fig. S 9).

		Asym. Al(IV)a		Asym. Al(IV)b		Asym. Al(V)		Asym. Al(VI)a		Sym. Al(VI)b	
	Relative amount of Al species[a]	M-A-S-H		MK or zeolitic precursor		MK		M-A-S-H/hydrotalcite/Al(OH)$_3$		M-A-S-H/hydrotalcite	
		δiso	Rel. amount[b]	δiso	Rel. amount[b]	δiso	Rel. amount[b]	δiso	Rel. amount[b]	δiso	Rel. amount[b]
		ppm	[%]	ppm	[%]	ppm	[%]	ppm	[%]	ppm	[%]
MK		67	36			38	53	10	11		
MASH[c]		69	40					12	27	9	33
AMS	28 d	67	36			36	6	11	13	9	45
	182 d	51.2	66	34			37	4	11	17	9	45
H-AMS	28 d	65	24			35	18	11	23	9	35
	182 d	40.2	66	25			35	18	13	22	9	35
3AMS	28 d	71	27			28	8	13	40	9	25
	182 d	100.0	70	27			30	7	14	43	9	23
H-3AMS	28 d	74	19	56	6	32	12	15	52	9	11
	182 d	88.4	73	19	56	5	30	11	14	47	9	18

[a] relative amount of Al species = absolute signal intensity normalized by the amount of material and number of scans.

[b] relative amount = from the line shape analysis for a total of 100%, need to be corrected to the relative amount of Al species for comparison.

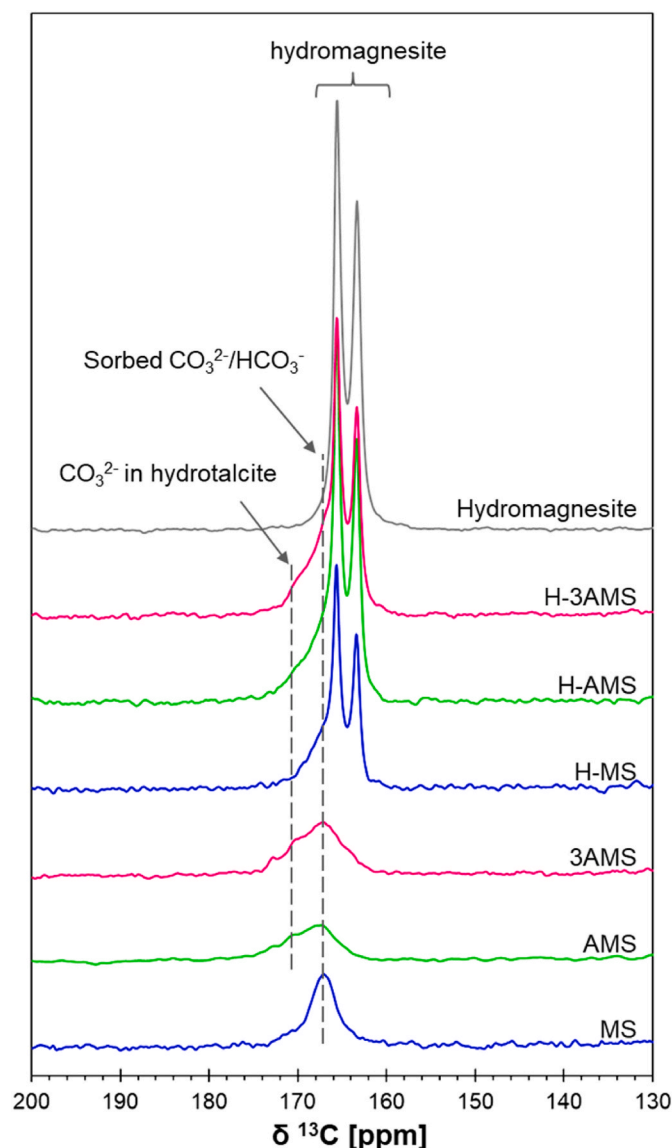[c] pure M-A-S-H phase with Mg/Si = 1.1, Al/Si = 0.15 [33].

Fig. 7. Region of carboxylate species of ^{13}C CP MAS NMR spectra of 182 days old samples prepared without (samples MS, AMS, 3AMS) and with hydromagnesite (samples H-MS, H-AMS and H-3AMS)) as starting material (spectrum of pure HY shown at top). MS and H-MS data from Ref. [30].

12 and 9 ppm, respectively, and of ~40% of Al(IV) at 69 ppm, but no evidence of aluminium in pentahedral environment because metakaolin has been added in lower quantity and had completely reacted [33]. In this study, residual unreacted metakaolin in 28 days or 182 days old samples can be detected by the appearance of residual signal intensity in the region around 35-20 ppm attributable to asymmetric Al(V) species. The highest amount of unreacted metakaolin was observed in the hydromagnesite containing samples H-AMS and H-3AMS (Table 5), while in the hydromagnesite free samples (AMS and 3AMS) this starting material has largely disappeared.

The resonance Al(IV)$_a$ at 66–69 ppm has been attributed to M-A-S-H and the signals Al(VI)$_a$ and Al(VI)$_b$ to M-A-S-H and hydrotalcite or Al(OH)$_3$, respectively [20,33,41]. More hydrotalcite/Al(OH)$_3$ is observed for the more Al rich samples 3AMS and H-3AMS. For those samples in addition a deshielding (shift to higher δ_{iso} of 70–74 ppm) is observed for Al(IV)$_a$ in M-A-S-H, which could be related to a change of Al(IV) environment, such as an increased amount of Al in the silicate layer and/or the replacement of Na $^+$ by Mg^{2+} ions in the Stern/diffusive layers of M-A-S-H [78].

The highest relative amounts of Al(VI)$_a$ indicating the presence of more M-A-S-H and Al(OH)$_3$ are observed in the samples AMS and 3AMS. In the samples containing hydromagnesite, lower amounts of Al(VI)$_a$ are found indicating the formation of less M-A-S-H, probably due to the lower reaction degree of the metakaolin as indicated by the presence of Al(V) species or Q^A and Q^B in the ^{29}Si MAS NMR data. The relatively high amount of Al(VI)$_a$ to Al(IV)$_a$ amount in the 3AMS and H-3AMS samples seems to indicate the presence of significant amounts of Al(OH)$_3$. The H–Si MAS NMR data indicate a relatively low content of M-(A-)S–H in the 3AMS sample (~40% lower than in the AMS sample). Thus the Al in the asymmetric Al(VI)$_a$ configuration can be attributed mainly to amorphous AlO(OH)/Al$_2$O$_3$/Al(OH)$_3$ in the case of the 3AMS and H-3AMS samples confirming the presence of amorphous hydroxy aluminate as already observed by XRD.

The broad resonances of Al(IV)$_b$ (δ_{iso} of 56 ppm) can be related to the high quantity of unreacted metakaolin as observed in the ^{29}Si MAS NMR data. From ^{27}Al NMR chemical shift of Al(IV)$_b$ the presence of a zeolitic precursor (or a N-A-S-H phase) could also be possible. Since no clear indications were found in the ^{29}Si MAS NMR data nor in the data from other techniques, the possible formation of a zeolitic phase remains unclear.

3.4. ^{13}C CP MAS NMR and ^{23}Na MAS NMR data

In the ^{13}C CP MAS NMR spectra, all resonances were observed within the narrow chemical shift range from 160 to 175 ppm, typical for carboxyl and carbonate compounds (Fig. 7). The spectrum of pure hydromagnesite showed two narrow resonances at 165.6 and 163.4 ppm as already reported [79]. These signals were observed in the ^{13}C MAS NMR spectra after 182 days in all samples prepared with hydromagnesite as starting material (Fig. 7b, "H" samples), indicating only partial hydromagnesite reaction. Additionally, in the ^{13}C NMR spectra of the aged samples, broad signals can be recognized at the base of the resonances of hydromagnesite.

The individual spectra were analysed by line shape simulations (for details see section 2.3.5). The results of the deconvolutions of the ^{13}C NMR data are summarized in Table 6 and an example including the simulated signals is shown in Fig. S10. In the ^{13}C MAS NMR spectrum of a crystalline sample of CO$_3$-hydrotalcite (Fig. S11), a narrow signal was observed at 170.7 ppm, which can be attributed to CO$_3^{2-}$ in the interlayer of the material [80]. Since the investigated reference sample was very pure and highly crystalline, the observed signal was very narrow (line width of 170 Hz) (Fig. S11). The rather broad resonances observed at 170 ppm in aged samples of this study (Fig. 7 and Table 6) are therefore attributed to carbonate species in a poorly crystalline hydrotalcite phase. Ishihara et al. [81] have described that in hydrotalcite, in addition to the signal at 170 ppm, a broad resonance can occur at 167 ppm, which they have assigned to HCO$_3^-$ in the interlayer. However, in the region of 167 ppm also broad peaks from HCO$_3^-$/CO$_3^{2-}$ sorbed on M-S-H can be observed [30]. The broad ^{13}C NMR resonance observed at 167 ppm in our aged samples (Table 6) may thus be assigned to HCO$_3^-$/CO$_3^{2-}$ present at surface of hydrotalcite, M-S-H or other solids.

The ^{23}Na MAS NMR spectra of the samples aged of 182 days are displayed in Fig. S12. All ^{23}Na NMR resonances are observed in the narrow range of −2.7 ± 1 ppm, the signals are symmetrical and relatively narrow ($\Delta\nu_{1/2} \approx 362$–850 Hz). This indicates, the presence of fully hydrated sodium (Na(H$_2$O)$_x^+$) in the solution, as discussed in Ref. [30]. In suspension, hydrated sodium (Na(H$_2$O)$_x^+$) sorbed at the cation exchange surface sites of M-S-H presents a broader resonance at −5.8 ± 1 ppm [41]. The relative amounts of sodium species are summarized in Table S3. The sodium content in the samples were found similar in all samples (85–100%) except for the H-3AMS sample, where only half of the sodium were found, which could be related to the low amount of M-A-S-H and hydrotalcite formed in that system. This indicated that most of the sodium initially added was located in the diffuse layers of the hydrated phases, most likely around the M-(A-)S–H phases except in

Table 6
^{13}C CP MAS NMR data: chemical shift assignments and relative amounts of carboxyl species determined by the deconvolution of the ^{13}C CP MAS NMR spectra (^{13}C CP MAS NMR spectra shown in Fig. 7, example of deconvolutions shown in Fig. S 10) and amount of hydromagnesite in the carboxyl species, expressed in % and in g/100g and degree of reaction of the hydromagnesite estimated by the ^{13}C CP MAS NMR data.

	Relative amount of carboxyl species[a]	CO_3^{2-} in poorly crystalline hydrotalcite		Sorbed HCO_3^-/CO_3^{2-}		hydromagnesite resonance A		hydromagnesite resonance B					
		δ [13]C [ppm]	relative amount[b] [%]	δ [13]C [ppm]	relative amount[b] [%]	δ [13]C [ppm]	relative amount[b] [%]	δ [13]C [ppm]	relative amount[b] [%]	ratio A/B	**Total of HY [%]**	HY (g/100g dry binder[c])	Reaction of HY (%)
hydromagnesite (HY)	100					165.6	53.8	163.4	46.2	0.9	100		
CO_3-hydrotalcite	–	170.8	100										
MS	8.0			167.1	100.0								
H-MS	16.2			167.1	37.3	165.6	35.6	163.4	27.1	0.8	**62.7**	**7.6**	**74**
AMS	6.4	170.0	58.8	167.1	41.2								
H-AMS	27.4	170.0	13.2	167.1	23.4	165.6	34.9	163.4	28.5	0.8	**63.5**	**14.2**	**34**
3AMS	9.0	170.0	42.8	167.1	57.2								
H-3AMS	23.6	170.0	11.4	167.1	31.8	165.6	31.4	163.4	25.4	0.8	**56.8**	**10.7**	**45**

[a] relative amount of carboxyl species = absolute signal intensity normalized by the amount of material and number of scans.

[b] relative amount = from the line shape analysis for a total of 100%.

[c] H-MS, H-AMS and H-3AMS samples contain 29.3, 21.5 and 19.3 g of hydromagnesite per 100 g of dry binder, respectively.

Table 7
pH ($\pm$0.2, mean of 6 measurements) of the leached solutions (measured at 23 °C) for the samples aged for 182 days.

	pH
3AMS	10.7
AMS	10.4
MS	9.8
H-3AMS	9.8
H-AMS	9.8
H-MS	9.7

the case of the H-3AMS sample, where only small amount of M-(A-)S–H were formed (as detailed by the H–Si CP NMR data).

3.5. pH values of the leached solutions

The pH values of the leached solutions for the 182 days old samples are summarized in Table 7. The pH values of 9.8 and 9.7 determined for the MS and H-MS samples, respectively, confirmed an environment where brucite is unstable, but the formation of M-S-H is favoured [43, 82]. The pH of the leached solutions of the AMS and 3AMS samples were about 10.4 and 10.7, respectively, slightly higher than the pH of the MS sample even if metakaolin was still present in the sample. This higher pH could be due to the residual traces of MgO found in the two samples after 182 days, which controlled the pH during the leaching experiments by hydrating into $Mg(OH)_2$ or due to the formation of additional hydrotalcite containing carbonates. The H-AMS and H-3AMS samples presented a similar pH to the H-MS samples, indicating that the presence of hydromagnesite dominates the pH of the leached solution.

4. Phase assemblages, thermodynamic modelling and mechanical properties

4.1. MS, AMS and 3AMS samples

In the absence of Al, M-S-H precipitation is accelerated in the presence of Na_2CO_3 as detailed in Ref. [30]. The MgO and the silica fume in the MS sample were 95% reacted after 28 days and fully reacted after 182 days. The M-S-H of this study exhibited a Mg/Si $\simeq$ 1.5 and T:O structure with mainly Mg^{2+} and complexes Mg^{2+}-carbonates at the exchangeable sites.
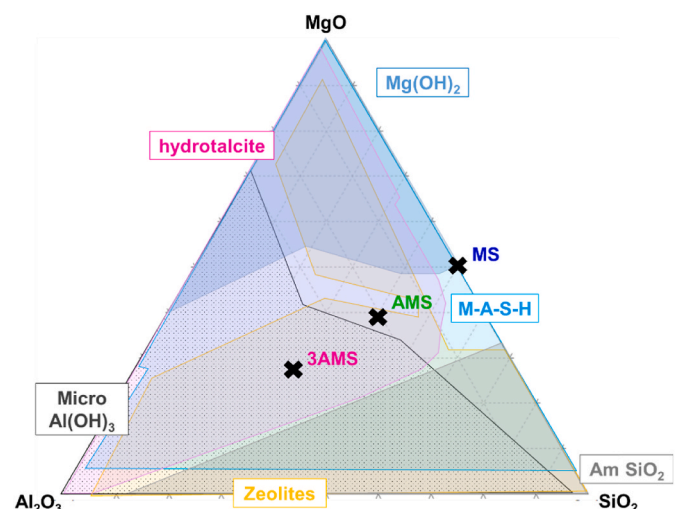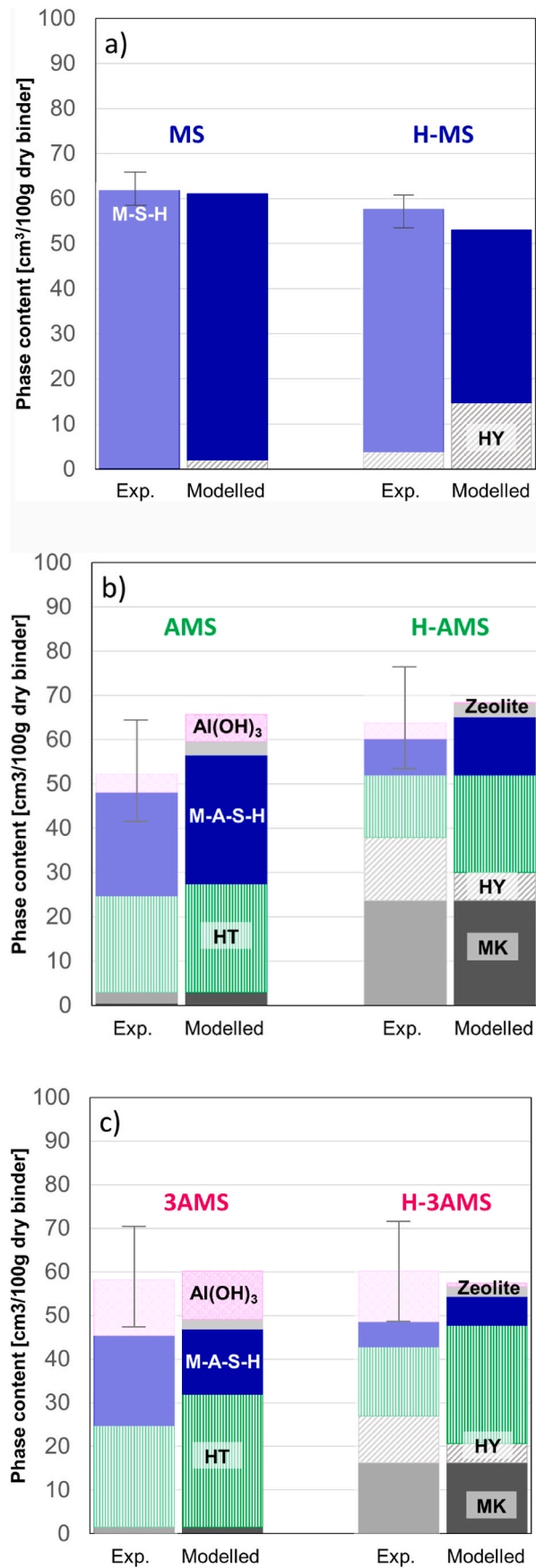

Fig. 8. $MgO–Al_2O_3–SiO_2$ ternary plot of the phase assemblage predicted by thermodynamic modelling in presence of Na_2CO_3 (1.7 g) and H_2O (100 g) as in the experimental conditions. Zeolites = mordenite-Na, natrolite, chabazite-Na, sodalite-Na or zeolite 4 Å.

In the presence of alumina and less MgO (AMS and 3AMS samples), hydrotalcite was observed after 3 days by XRD, TGA and ^{27}Al MAS NMR data in addition to M-(A-)S–H. At early age, some more unreacted MgO remained compared to the MS samples even if the MgO content was initially lower. This lower reaction degree could be related to the higher pH of the AMS and 3AMS samples compared to the MS system.

After 28 days, the degree of MK reaction in the AMS and 3AMS samples was found to be above 80% which stayed more or less constant afterwards (^{29}Si and ^{27}Al MAS NMR data), while most MgO had reacted (residual MgO $\leq$2 wt %, based on XRD data). Only traces of brucite were observed (much less than in the MS sample) which could be related to the formation of hydrotalcite in the presence of alumina.

In the 3AMS samples, which contained the highest initial content of alumina, alumina reacted only partially into the hydrotalcite and M-(A-)S–H phases, while in addition, a significant amount of AlO(OH) and/or $Al(OH)_3$ formed (XRD and ^{27}Al MAS NMR data).

The amount and kind of hydrotalcite could not be characterised by XRD due to its poorly crystalline nature. However, a hydrotalcite with a low Mg/Al ratio of 2 can be expected due to the rather high amount of

alumina. Also the presence of CO_3^{2-} in the interlayer most likely occurs due to the high stability of CO$_3$-bearing hydrotalcite [20] and presence of carbonates in the solid phase as shown by the broad resonance at 170 ppm in ^{13}C NMR spectra.

The ternary diagram shown in Fig. 8 illustrates the calculated thermodynamic stability of the system Al$_2$O$_3$–MgO–SiO$_2$ in the presence of 1.7 g of sodium carbonate per 100 g of binder. The compositions of the MS, AMS and 3AMS samples assuming complete reaction are indicated by crosses. For the modelling, the formation of crystalline zeolites was applied as a proxy for poorly crystalline N-A-S-H phases, due to the limited availability of thermodynamic data for the latter phases.

M-(A-)S–H was predicted to be stable at most conditions, together with brucite in the presence of a surplus of MgO or amorphous silica at the Si-rich end. The presence of alumina is expected to lead in addition to the formation of hydrotalcite [20] and zeolites; mordenite-Na, natrolite, chabazite-Na, sodalite-Na or zeolite 4 Å were stable in most cases.

The modelling indicated the formation of M-S-H and possibly traces of brucite for the MS sample, which agrees well with the experimental observations. The thermodynamic modelling for the AMS sample indicates the formation of M-A-S-H, hydrotalcite and zeolites (possible zeolites are detailed in the capture of Fig. 8) and, in addition, the precipitation of microcrystalline Al(OH)$_3$ for the 3AMS sample. This corresponds to the experimental observations, with the exception of zeolites (which are a proxy N-A-S-H phases), which could not clearly be identified although a minor amount of N-A-S-H phases might be present or will form in the long term as e.g. observed in Ref. [61].
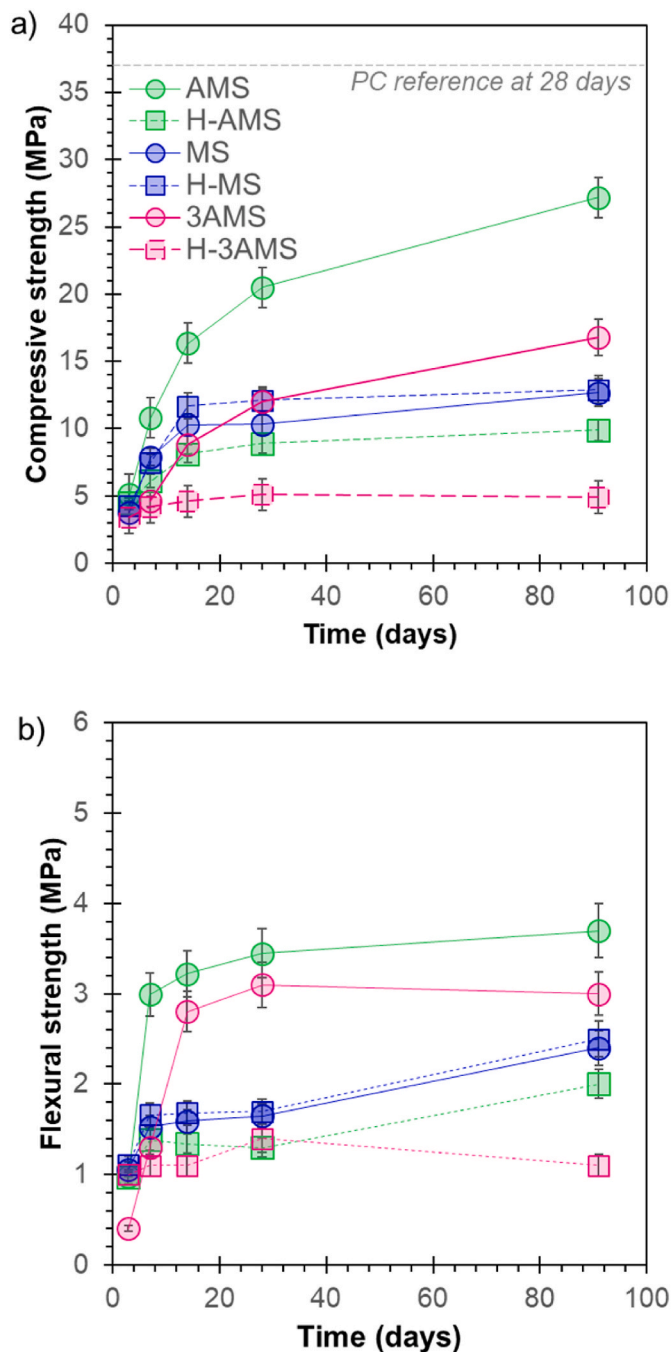
The modelled phase assemblages and the associated calculated volumes are presented in Fig. 9 together with experimental results estimated from the NMR data. In general, the predicted and observed phases reasonably agreed, although the formation of hydromagnesite was predicted for MS sample, but not observed experimentally. This could be related to the sensitivity of the experimental characterisations. Quantitative comparison with Al-containing samples is difficult due to high error associated with the experimental data due to the impossibility to estimate the quantities of the N-A-S-H phases and the difficulties in deconvoluting reliably the Al NMR data.

The compressive strengths of the MS and the AMS and 3AMS samples for up to 91 days are shown in Fig. 10. The AMS mortar showed the highest compressive strength up to 27 MPa after 91 days, while the compressive strengths of the MS and 3AMS mortars were with 13 MPa and 17 MPa after 91 days lower than the AMS mortar. The order of the measured compressive strength agreed with the order of the porosities of 43%, 51% and 52% for the AMS, 3AMS and MS mortars, respectively, calculated by thermodynamic modelling (Table S4). The addition of an intermediate amount of aluminium (Al/Si = 1 Mg/Al = 1.5) seemed to improve the mechanical properties due to the precipitation of hydrotalcite decreasing the porosity of the system. However, higher amounts of aluminium (Al/Si = 3.2 Mg/Al = 2.5) led to less silica, decreasing the amount of M-A-S-H and increasing the porosity, and thus resulting in lower mechanical strength.

4.2. H-MS, H-AMS and H-3AMS samples

The H-MS sample showed a slightly lower Mg/Si in the M-S-H than the MS sample about $\simeq$ 1.4 due to the presence of unreacted

"modelled" in Fig. 9a), while the experimental solid volume decreased by about 7% (see "Exp." in Fig. 9a). This changes in solid volume, however, had little effect on compressive strength; both the MS and H-MS samples showed similar compressive and flexural strengths over time (e.g. for compressive strengths: 4.1 ± 0.3 MPa after 3 days and 12.8 ± 0.3 MPa after 91 days, see Fig. 10a). Taking into account the w/s of 0.9, the phase assemblage and the molar volume of M-S-H and hydro-magnesite, a total porosity of about 55 and 59 vol% was experimentally observed for the MS and H-MS samples, respectively [30].

In presence of alumina, the main reaction products are M-(A-)S–H and hydrotalcite, but unreacted hydromagnesite and unreacted alumina (metakaolin or amorphous Al_2O_3) both are still present in the samples. The reaction degree of the hydromagnesite was about 35–45 wt % ([13]CP MAS NMR, Table 6) and about 20–50 wt % of the MK (^{29}Si MAS NMR data, Table 4) had reacted. The lower pH of the H-samples (9.8) compared to the hydromagnesite-free samples ($\geq$10.4) might be the cause of the lower reaction degree as metakaolin usually dissolves faster at higher pH [83].

The hydromagnesite and aluminium containing samples (H-AMS and H-3AMS) showed lower mechanical properties than the hydromagnesite-free samples (AMS and 3AMS), as the hydromagnesite hardly reacted leading to lower M-(A-)S–H formation and, presumably the presence of hydromagnesite additionally, lowered the reactivity of the metakaolin. Among the hydromagnesite containing samples, H-AMS mortar showed the highest compressive strength, reaching 10 MPa after 91 days, which is 3 times lower than the strength determined for the AMS mortar (no hydromagnesite). The H-3AMS mortar showed an even lower compressive strength of 5 MPa after 91 days. The calculated po-rosities modelled by thermodynamic considerations (Table S4) were equal to 55 and 61 vol% for the H-AMS and the H-3AMS samples, respectively. The presence of hydromagnesite (H-samples) increased the porosity by about 5 vol% compared to MS, AMS and 3AMS. Whereas no significant effect on the strength of H-MS samples was observed the strengths determined for the H-AMS and H-3AMS samples decreased by a factor of ~3 compared to the AMS and 3AMS samples. The reason for this different behaviour is presently not known.

5. Conclusions

In this study, the effect of large quantities of alumina and carbonates in magnesium silicate cement on M-S-H precipitation was studied. Na_2CO_3 or hydromagnesite were used as carbonate sources and Na_2CO_3 solution acted as an activator. The presence of alumina and carbonates seemed to prevent the precipitation of $Mg(OH)_2$ and favoured the for-mation of hydrotalcite and M-(A-)S–H. Higher contents of Al decreased the early consumption of MgO and favoured the formation of hydro-talcite, but also the non-reaction of AlO(OH) and formation of $Al(OH)_3$ and therefore, lowered the amount of M-(A-)S–H. Over time, the quan-tity and/or the crystallinity of hydrotalcite increased as evidenced by X-ray diffraction.

The presence of hydromagnesite did not significantly accelerate the reactions, but lowered the consumption of metakaolin to 20–50%, and only little reactions of hydromagnesite (40–50 wt %) was observed. The reduced reactivity of metakaolin could potentially be related to the lower pH in the solution.

The highest compressive strength (25–30 MPa) wass obtained for the AMS sample (i.e. Mg/Si = 1.5 and Al/Si = 1), while the presence of more alumina in the 3AMS sample (i.e. Mg/Si = 2.5 and Al/Si = 3.2) lowered the mechanical strength to the order of magnitude of the Al-free sample (MS and H-MS). Note that the water/solid (w/s) was set at 0.9. However, the w/s was not optimized, and much higher compressive strength could be achieved if the w/s value would be greatly reduced by optimizing kind and content of superplasticizer.

The best compressive strength for the binder containing an inter-mediate amount of alumina and no hydromagnesite (sample AMS), was mostly obtained due to the reaction of MgO and metakaolin to

Fig. 10. a) Compressive and b) flexural strengths at 3, 7, 14, 28 and 91 days for the MS/H-MS (blue), AMS/H-AMS (green) and 3AMS/H-3AMS (pink) mortars. PC reference at 28 days indicates the compressive strength of Portland mortars after 28 days. (For interpretation of the references to colour in this figure legend, the reader is referred to the Web version of this article.)

hydromagnesite (degree of reaction of hydromagnesite ~ 70%), while silica fume had fully reacted as fully detailed in Ref. [30]. Thermody-namic modelling (see Fig. 9a) predicted less reaction of hydromagnesite than experimentally observed for H-MS and the precipitation of small amount of hydromagnesite in the case of the MS sample, which was not observed. This may indicate that the thermodynamic data overestimate the stability of hydromagnesite, that an additional, not identifed phase had formed or that the sorption of carbonate on the surface of M-S-H (which was not considered in the model) could be able to destabilise hydromagnesite. The total phase volume predicted by thermodynamic modelling was decreased by 13% from the MS to the H-MS sample (see

hydrotalcite and M-(A-)S–H. A further increase of alumina content, however, led to the formation of increased amount of amorphous Al (OH)$_3$, which did not seem to improve the mechanical properties.

Finally, the use of metakaolin instead of silica fume in M-S-H binder system leads the formation of M-S-H with incorporation of aluminium and the formation of hydrotalcite but no Mg-carbonate could be observed. The stability of the Al$_2$O$_3$–MgO–SiO$_2$–CO$_2$–H$_2$O system adds more complexity to the M-S-H binder and would need further investigations.

Declaration of competing interest

The authors declare the following financial interests/personal relationships which may be considered as potential competing interests: Ellina Bernard reports financial support was provided by Swiss National Science Foundation.

Data availability

Data will be made available on request.

Acknowledgements

Appendix A. Supplementary data

Supplementary data to this article can be found online at https://doi.org/10.1016/j.cemconcomp.2023.105010.

References

[1] S.A. Miller, A. Horvath, P.J. Monteiro, Readily implementable techniques can cut annual CO$_2$ emissions from the production of concrete by over 20, Environ. Res. Lett. 11 (2016), 074029.

[2] P. Sargent, The development of alkali-activated mixtures for soil stabilisation, Handbook of alkali-activated cements, mortars and concretes, Elsevier (2015) 555–604.

[3] J.L. Provis, K. Arbi, S.A. Bernal, D. Bondar, A. Buchwald, A. Castel, S. Chithiraputhiran, M. Cyr, A. Dehghan, K. Dombrowski-Daube, RILEM TC 247-DTA round robin test: mix design and reproducibility of compressive strength of alkali-activated concretes, Mater. Struct. 52 (2019) 1–13.

[4] J.L. Provis, Alkali-activated materials, Cement Concr. Res. 114 (2018) 40–48.

[5] G. Habert, J.D.E. De Lacaillerie, N. Roussel, An environmental evaluation of geopolymer based concrete production: reviewing current research trends, J. Clean. Prod. 19 (2011) 1229–1238.

[6] G. Kastiukas, S. Ruan, S. Liang, X. Zhou, Development of precast geopolymer concrete via oven and microwave radiation curing with an environmental assessment, J. Clean. Prod. 255 (2020), 120290.

[7] C.-L. Hwang, D.-H. Vo, V.-A. Tran, M.D. Yehualaw, Effect of high MgO content on the performance of alkali-activated fine slag under water and air curing conditions, Construct. Build. Mater. 186 (2018) 503–513.

[8] S. Ruan, S. Liang, G. Kastiukas, W. Zhu, X. Zhou, Solidification of waste excavation clay using reactive magnesia, quicklime, sodium carbonate and early-age oven curing, Construct. Build. Mater. 258 (2020), 120333.

[9] S. Ruan, C. Unluer, Comparative life cycle assessment of reactive MgO and Portland cement production, J. Clean. Prod. 137 (2016) 258–273.

[10] A. Scott, C. Oze, V. Shah, N. Yang, B. Shanks, C. Cheeseman, A. Marshall, M. Watson, Transformation of abundant magnesium silicate minerals for enhanced CO2 sequestration, Commun. Earth. Environ. 2 (2021) 25.

[11] R. Zevenhoven, M. Slotte, E. Koivisto, R. Erlund, Serpentinite carbonation process routes using ammonium sulfate and integration in industry, Energy Technol. 5 (2017) 945–954.

[12] B. Lothenbach, F. Winnefeld, Thermodynamic modelling of the hydration of Portland cement, Cement Concr. Res. 36 (2006) 209–226.

[13] S.A. Bernal, R. San Nicolas, R.J. Myers, R.M. de Gutiérrez, F. Puertas, J.S. van Deventer, J.L. Provis, MgO content of slag controls phase evolution and structural changes induced by accelerated carbonation in alkali-activated binders, Cement Concr. Res. 57 (2014) 33–43.

[14] R.J. Myers, B. Lothenbach, S.A. Bernal, J.L. Provis, Thermodynamic modelling of alkali-activated slag cements, Appl. Geochem. 61 (2015) 233–247.

[15] S. Park, H.M. Park, H. Yoon, J. Seo, C.-M. Yang, J.L. Provis, B. Yang, Hydration kinetics and products of MgO-activated blast furnace slag, Construct. Build. Mater. 249 (2020), 118700.

[16] S.M. Park, J. Jang, H.-K. Lee, Unlocking the role of MgO in the carbonation of alkali-activated slag cement, Inorg. Chem. Front. 5 (2018) 1661–1670.

[17] M.B. Haha, B. Lothenbach, G. Le Saout, F. Winnefeld, Influence of slag chemistry on the hydration of alkali-activated blast-furnace slag—Part I: effect of MgO, Cement Concr. Res. 41 (2011) 955–963.

[18] S. Miyata, Anion-exchange properties of hydrotalcite-like compounds, Clay Clay Miner. 31 (1983) 305–311.

[19] D.P. Prentice, L. Gomez-Zamorano, M. Balonis, B. Erdemli, K. Ellison, N. Neithalath, D. Simonetti, G. Sant, The Effects of (Di-, Tri-valent)-cation Partitioning and Intercalant Anion-type on the Solubility of Hydrotalcites, Journal of the American Ceramic Society, 2020.

[20] E. Bernard, B. Lothenbach, W.J. Zucha, U. Mäder, Stability of hydrotalcite (Mg-Al layered double hydroxide) in presence of different anions, Cement Concr. Res. 152 (2022), 106674.

[21] A. Abdalqader, F. Jin, A. Al-Tabbaa, Performance of magnesia-modified sodium carbonate-activated slag/fly ash concrete, Cement Concr. Compos. 103 (2019) 160–174.

[22] T. Zhang, C. Cheeseman, L. Vandeperre, Development of low pH cement systems forming magnesium silicate hydrate (MSH), Cement Concr. Res. 41 (2011) 439–442.

[23] S.A. Walling, H. Kinoshita, S.A. Bernal, N.C. Collier, J.L. Provis, Structure and properties of binder gels formed in the system Mg(OH)$_2$-SiO$_2$-H$_2$O for immobilisation of Magnox sludge, Dalton Trans. 44 (2015) 8126–8137.

[24] S.A. Walling, H. Kinoshita, N. Bryan, Magnesium silicate hydrate cement for magnox sludge encapsulation, in: 32nd Cement and Concrete Science Conference, 2012, p. 180.

[25] T. Zhang, T. Li, J. Zou, Y. Li, S. Zhi, Y. Jia, C.R. Cheeseman, Immobilization of radionuclide ^{133}Cs by magnesium silicate hydrate cement, Materials 13 (2020) 146.

[26] T. Zhang, L.J. Vandeperre, C.R. Cheeseman, Magnesium-silicate-hydrate cements for encapsulating problematic aluminium containing wastes, J. Sustain. Cement-Based Mater. 1 (2012) 34–45.

[27] M.R. Marsiske, C. Debus, F. Di Lorenzo, E. Bernard, S.V. Churakov, C. Ruiz-Agudo, Immobilization of (aqueous) cations in low pH MSH cement, Appl. Sci. 11 (2021) 2968.

[28] T. Zhang, L.J. Vandeperre, C.R. Cheeseman, Formation of magnesium silicate hydrate (MSH) cement pastes using sodium hexametaphosphate, Cement Concr. Res. 65 (2014) 8–14.

[29] C. Sonat, W. Teo, C. Unluer, Performance and microstructure of MgO-SiO$_2$ concrete under different environments, Construct. Build. Mater. 184 (2018) 549–564.

[30] E. Bernard, B. Lothenbach, D. Rentsch, A. German, F. Winnefeld, Effect of carbonated sources on magnesium silicate hydrate (M-S-H), Mater. Struct. 55 (2022) 183.

[31] V. Shah, A. Scott, Use of kaolinite clays in development of a low carbon MgO-clay binder system, Cement Concr. Res. 144 (2021), 106422.

[32] M. Dhakal, A.N. Scott, V. Shah, R.P. Dhakal, D. Clucas, Development of a MgO-metakaolin binder system, Construct. Build. Mater. 284 (2021), 122736.

[33] E. Bernard, B. Lothenbach, C. Cau-Dit-Coumes, I. Pochard, D. Rentsch, Aluminum incorporation into magnesium silicate hydrate (M-S-H), Cement Concr. Res. 128 (2020), 105931.

[34] V. Shah, A. Scott, Hydration and microstructural characteristics of MgO in the presence of metakaolin and silica fume, Cement Concr. Compos. 121 (2021), 104068.

[35] V. Shah, Y. Dhandapani, A. Scott, Pore structure characteristics of MgO–SiO2 binder, J. Am. Ceram. Soc. 104 (2021) 6002–6014.

[36] K. Khan, M.F. Ullah, K. Shahzada, M.N. Amin, T. Bibi, N. Wahab, A. Aljaafari, Effective use of micro-silica extracted from rice husk ash for the production of high-performance and sustainable cement mortar, Construct. Build. Mater. 258 (2020), 119589.

[37] A. Tafraoui, G. Escadeillas, T. Vidal, Durability of the ultra high performances concrete containing metakaolin, Construct. Build. Mater. 112 (2016) 980–987.

[38] K. Scrivener, F. Martirena, S. Bishnoi, S. Maity, Calcined clay limestone cements (LC3), Cement Concr. Res. 114 (2018) 49–56.

[39] E. Bernard, B. Lothenbach, A. German, F. Winnefeld, Effect of carbonates on the formation of magnesium silicate hydrates (M-S-H) and magnesium alumino silicate hydrates (M-A-S-H), Procced. Synercrete. 2023 (2023).

[40] D. Madej, C. Ortmann, J. Szczerba, M. Jacewicz, Calorimetry and other methods in the studies of reactive magnesia–hydratable alumina–microsilica hydrating mixtures, J. Therm. Anal. Calorimetry 126 (2016) 1133–1142.

[41] E. Bernard, B. Lothenbach, D. Rentsch, Influence of sodium nitrate on the phases formed in the MgO-Al$_2$O$_3$-SiO$_2$-H$_2$O system, Mater. Des. 198 (2021), 109391.

[42] S.A. Walling, S.A. Bernal, L.J. Gardner, H. Kinoshita, J.L. Provis, Phase Formation and evolution in Mg (OH)$_2$–Zeolite cements, Ind. Eng. Chem. Res. 57 (2018) 2105–2113.

[43] D. Nied, K. Enemark-Rasmussen, E. L'Hopital, J. Skibsted, B. Lothenbach, Properties of magnesium silicate hydrates (MSH), Cement Concr. Res. 79 (2016) 323–332.

[44] C. Roosz, S. Grangeon, P. Blanc, V. Montouillout, B. Lothenbach, P. Henocq, E. Giffaut, P. Vieillard, S. Gaboreau, Crystal structure of magnesium silicate

hydrates (MSH): the relation with 2: 1 Mg–Si phyllosilicates, Cement Concr. Res. 73 (2015) 228–237.

[45] A. Machner, M. Zajac, M.B. Haha, K.O. Kjellsen, M.R. Geiker, K. De Weerdt, Limitations of the hydrotalcite formation in Portland composite cement pastes containing dolomite and metakaolin, Cement Concr. Res. 105 (2018) 1–17.

[46] F. Winnefeld, E. Epifania, F. Montagnaro, E.M. Gartner, Further studies of the hydration of MgO-hydromagnesite blends, Cement Concr. Res. 126 (2019), 105912.

[47] E. Bernard, B. Lothenbach, D. Rentsch, I. Pochard, A. Dauzères, formation of magnesium silicate hydrates (M-S-H), physics and chemistry of the Earth, Parts A/ B/C 99 (2017) 142–157.

[48] R. Snellings, J. Chwast, Ö. Cizer, N. De Belie, Y. Dhandapani, P. Durdzinski, J. Elsen, J. Haufe, D. Hooton, C. Patapy, RILEM TC-238 SCM recommendation on hydration stoppage by solvent exchange for the study of hydrate assemblages, Mater. Struct. 51 (2018) 1–4.

[49] B.H. O'Connor, M.D. Raven, Application of the Rietveld refinement procedure in assaying powdered mixtures, Powder Diffr. 3 (1988) 2–6.

[50] D. Jansen, F. Goetz-Neunhoeffer, C. Stabler, J. Neubauer, A remastered external standard method applied to the quantification of early OPC hydration, Cement Concr. Res. 41 (2011) 602–608.

[51] D. Massiot, F. Fayon, M. Capron, I. King, S. Le Calvé, B. Alonso, J.O. Durand, B. Bujoli, Z. Gan, G. Hoatson, Modelling one-and two-dimensional solid-state NMR spectra, Magn. Reson. Chem. 40 (2002) 70–76.

[52] D.R. Neuville, L. Cormier, D. Massiot, Al environment in tectosilicate and peraluminous glasses: a ^{27}Al MQ-MAS NMR, Raman, and XANES investigation, Geochem. Cosmochim. Acta 68 (2004) 5071–5079.

[53] J. Cui, D.L. Olmsted, A.K. Mehta, M. Asta, S.E. Hayes, NMR crystallography: evaluation of hydrogen positions in hydromagnesite by 13C {1H} REDOR solid-state NMR and density functional theory calculation of chemical shielding tensors, Angew. Chem. Int. Ed. 58 (2019) 4210–4216.

[54] R.K. Harris, E.D. Becker, S.M.C. De Menezes, R. Goodfellow, P. Granger, NMR nomenclature. Nuclear spin properties and conventions for chemical shifts (IUPAC Recommendations 2001), Pure Appl. Chem. 73 (2001) 1795–1818.

[55] G. Plusquellec, M. Geiker, J. Lindgård, J. Duchesne, B. Fournier, K. De Weerdt, Determination of the pH and the free alkali metal content in the pore solution of concrete: review and experimental comparison, Cement Concr. Res. 96 (2017) 13–26.

[56] M. Alonso, C. Garcia, J.L.C. Walker, M. Naito, S. Pettersson, I. Puigdomenech, M. A. Cuñado, M. Vuorio, H. Weber, H. Ueda, K. Fujisaki, Development of an Accurate pH Measurement Methodology for the Pore Fluids of Low pH Cementitious Materials, Swedish Nuclear Fuel and Waste Management Co., Stockholm (Sweden), 2012. www.skb.se/upload/publications/pdf/R-12-02.pdf.

[57] D. Kulik, T. Wagner, S.V. Dmytrieva, G. Kosakowski, F. Hingerl, K.V. Chudnenko, U. Berner, GEM-Selektor geochemical modeling package: revised algorithm and GEMS3K numerical kernel for coupled simulation codes, Computat Geochem 17 (2013) 1–24.

[58] T. Wagner, D.A. Kulik, F.F. Hingerl, S.V. Dmytrieva, GEM-Selektor geochemical modeling package: TSolMod library and data interface for multicomponent phase models, Can. Mineral. 50 (2012) 1173–1195.

[59] T. Thoenen, W. Hummel, U. Berner, E. Curti, The PSI/Nagra Chemical Thermodynamic Database 12/07, PSI Report 14-04, Villigen PSI, Switzerland, 2014.

[60] B. Lothenbach, D.A. Kulik, T. Matschei, M. Balonis, L. Baquerizo, B. Dilnesa, G. D. Miron, R.J. Myers, Cemdata18: a chemical thermodynamic database for hydrated Portland cements and alkali-activated materials, Cement Concr. Res. 115 (2019) 472–506.

[61] B. Ma, B. Lothenbach, Synthesis, characterization, and thermodynamic study of selected Na-based zeolites, Cement Concr. Res. 135 (2020), 106111.

[62] R.A. Robie, B.S. Hemingway, Thermodynamic Properties of Minerals and Related Substances at 298.15 K and 1 Bar (105 Pascals) Pressure and at Higher Temperatures, US Government Printing Office, 1995.

[63] B. Lothenbach, L. Pelletier-Chaignat, F. Winnefeld, Stability in the system CaO–Al$_2$O$_3$–H$_2$O, Cement Concr. Res. 42 (2012) 1621–1634.

[64] A.L. Harrison, V. Mavromatis, E.H. Oelkers, P. Bénézeth, Solubility of the hydrated Mg-carbonates nesquehonite and dypingite from 5 to 35° C: implications for CO2 storage and the relative stability of Mg-carbonates, Chem. Geol. 504 (2019) 123–135.

[65] R. Hill, J. Canterford, F. Moyle, New data for lansfordite, Mineral. Mag. 46 (1982) 453–457.

[66] E. Königsberger, L.-C. Königsberger, H. Gamsjäger, Low-temperature thermodynamic model for the system Na2CO3– MgCO3– CaCO3– H2O, Geochem. Cosmochim. Acta 63 (1999) 3105–3119.

[67] H.C. Helgeson, Summary and critique of the thermodynamic properties of rock-forming minerals, Am. J. Sci. 278 (1978) 1–229.

[68] J.W. Johnson, E.H. Oelkers, H.C. Helgeson, SUPCRT92: a software package for calculating the standard molal thermodynamic properties of minerals, gases, aqueous species, and reactions from 1 to 5000 bar and 0 to 1000 C, Comput. Geosci. 18 (1992) 899–947.

[69] Q. Gautier, P. Bénézeth, V. Mavromatis, J. Schott, Hydromagnesite solubility product and growth kinetics in aqueous solution from 25 to 75 C, Geochem. Cosmochim. Acta 138 (2014) 1–20.

[70] G. Raade, Dypingite, a new hydrous basic carbonate of magnesium, from Norway, Am. Mineral.: J. Earth. Planetary Mater. 55 (1970) 1457–1465.

[71] S. Miyata, The syntheses of hydrotalcite-like compounds and their structures and physico-chemical properties—I: the systems Mg^{2+}-Al^{3+}-NO$_3^-$, Mg^{2+}-Al^{3+}-Cl$^-$, Mg^2$^+$-Al^{3+}-ClO$_4^-$, Ni^{2+}-Al^{3+}-Cl$^-$ and Zn $^{2+}$-Al $^{3+}$-Cl$^-$, Clay Clay Miner. 23 (1975) 369–375.

[72] Y. Zhang, J. Chang, J. Zhao, Y. Fang, Nanostructural characterization of Al (OH) 3 formed during the hydration of calcium sulfoaluminate cement, J. Am. Ceram. Soc. 101 (2018) 4262–4274.

[73] F. Rey, V. Fornés, J.M. Rojo, Thermal decomposition of hydrotalcites. An infrared and nuclear magnetic resonance spectroscopic study, J. Chem. Soc., Faraday Trans. 88 (1992) 2233–2238.

[74] J.M. Mejía, E. Rodríguez, R.M. de Gutiérrez, N. Gallego, Preparation and characterization of a hybrid alkaline binder based on a fly ash with no commercial value, J. Clean. Prod. 104 (2015) 346–352.

[75] B. Walkley, R. San Nicolas, M.-A. Sani, G.J. Rees, J.V. Hanna, J.S. van Deventer, J. L. Provis, Phase evolution of C-(N)-ASH/NASH gel blends investigated via alkali-activation of synthetic calcium aluminosilicate precursors, Cement Concr. Res. 89 (2016) 120–135.

[76] H. Sreenivasan, E. Adesanya, H. Niu, P. Perumal, A.M. Kantola, V.-V. Telkki, M. Huttula, W. Cao, J.L. Provis, M. Illikainen, Evidence of formation of an amorphous magnesium silicate (AMS) phase during alkali activation of (Na-Mg) aluminosilicate glasses, Cement Concr. Res. 145 (2021), 106464.

[77] E. Bernard, B. Lothenbach, C. Chlique, M. Wyrzykowski, A. Dauzères, I. Pochard, C. Cau-Dit-Coumes, Characterization of magnesium silicate hydrate (M-S-H), Cement Concr. Res. 116 (2019) 309–330.

[78] J. Sanz, J. Serratosa, Silicon-29 and aluminum-27 high-resolution MAS-NMR spectra of phyllosilicates, J. Am. Chem. Soc. 106 (1984) 4790–4793.

[79] J.K. Moore, J.A. Surface, A. Brenner, P. Skemer, M.S. Conradi, S.E. Hayes, Quantitative identification of metastable magnesium carbonate minerals by solid-state ^{13}C NMR spectroscopy, Environ. Sci. Technol. 49 (2015) 657–664.

[80] T.F. Sevelsted, D. Herfort, J. Skibsted, 13C chemical shift anisotropies for carbonate ions in cement minerals and the use of 13C, 27Al and 29Si MAS NMR in studies of Portland cement including limestone additions, Cement Concr. Res. 52 (2013) 100–111.

[81] S. Ishihara, P. Sahoo, K. Deguchi, S. Ohki, M. Tansho, T. Shimizu, J. Labuta, J. P. Hill, K. Ariga, K. Watanabe, Dynamic breathing of CO$_2$ by hydrotalcite, J. Am. Chem. Soc. 135 (2013) 18040–18043.

[82] E. Bernard, B. Lothenbach, F. Le Goff, I. Pochard, A. Dauzères, Effect of magnesium on calcium silicate hydrate (C-S-H), Cement Concr. Res. 97 (2017) 61–72.

[83] N. Granizo, A. Palomo, A. Fernandez-Jiménez, Effect of temperature and alkaline concentration on metakaolin leaching kinetics, Ceram. Int. 40 (2014) 8975–8985.